Chemical evolution from cores to disks

Visser, R.

3

The chemical history of molecules in circumstellar disks II: Gas-phase species

R. Visser, S. D. Doty and E. F. van Dishoeck
to be submitted

Abstract

Context. The chemical composition of a molecular cloud changes dramatically as it collapses to form a low-mass protostar and circumstellar disk. Two-dimensional (2D) chemodynamical models are required to properly study this process.

Aims. The goal of this work is to follow, for the first time, the chemical evolution in two dimensions all the way from a pre-stellar cloud into a circumstellar disk. Of special interest is the question whether the chemical composition of the disk is a result of chemical processing during the collapse phase, or whether it is determined by in situ processing after the disk has formed.

Methods. We combine a semi-analytical method to get 2D axisymmetric density and velocity structures with detailed radiative transfer calculations to get temperature profiles and UV fluxes. Material is followed in from the cloud to the disk and a full gas-phase chemistry network – including freeze-out onto and evaporation from cold dust grains – is evolved along these trajectories. The abundances thus obtained are compared to the results from a static disk model and to cometary observations.

Results. The chemistry during the collapse phase is dominated by a few key processes, such as the evaporation of CO or the photodissociation of H_2O. Depending on the physical conditions encountered along specific trajectories, some of these processes are absent. At the end of the collapse phase, the disk can thus be divided into zones with different chemical histories. The disk is found not to be in chemical equilibrium at the end of the collapse. We argue that comets must be formed from material with different chemical histories: some of it is strongly processed, some of it remains pristine. Variations between individual comets are possible if they formed at different positions or times in the solar nebula. The chemical zones in the disk and the mixed origin of the cometary material arise from the 2D nature of our model.

3.1 Introduction

The formation of a low-mass protostar out of a cold molecular cloud is accompanied by large-scale changes in the chemical composition of the constituent gas and dust. Pre-stellar cloud cores are cold (∼10 K), moderately dense (∼10^4–10^6 cm^{-3}), and irradiated only by the ambient interstellar radiation field (see reviews by Shu et al. 1987, di Francesco et al. 2007 and Bergin & Tafalla 2007). As the core starts to collapse, several mechanisms act to heat up the material, such as gravitational contraction, accretion shocks and, eventually, radiation produced by nuclear fusion in the protostar. The inner few hundred AU of the core flatten out to form a circumstellar disk, where planets may be formed at a later stage (see review by Dullemond et al. 2007b). The density in the interior of the disk, especially at small radii, is several orders of magnitude higher than the density of the pre-stellar core. Meanwhile, the protostar infuses the disk with high fluxes of ultraviolet and X-ray photons. The chemical changes arising from these evolving physical conditions have been analysed by various groups with one-dimensional models (see reviews by Ceccarelli et al. 2007, Bergin et al. 2007 and Bergin & Tafalla 2007). However, two-dimensional models are required to properly describe the formation of the circumstellar disk and the chemical processes taking place inside it.

This chapter follows the preceding chapter in a series of publications aiming to model the chemical evolution from pre-stellar cores to circumstellar disks in two dimensions. Chapter 2 contains a detailed description of our semi-analytical model and an analysis of the gas and ice abundances of carbon monoxide (CO) and water (H_2O). We found that most CO evaporates during the infall phase and freezes out again in those parts of the disk that are colder than 18 K. The much higher binding energy of H_2O keeps it in solid form at all times, except within ∼10 AU of the star. Based on the time that the infalling material spends at dust temperatures between 20 and 40 K, first-generation complex organic species were predicted to form abundantly on the grain surfaces according to the scenario of Garrod & Herbst (2006) and Garrod et al. (2008).

The current chapter extends the chemical analysis to a full gas-phase network, including freeze-out onto and evaporation from dust grains, as well as basic grain-surface hydrogenation reactions. Combining semi-analytical density and velocity structures with detailed temperature profiles from full radiative transfer calculations, our aim is to bridge the gap between 1D chemical models of collapsing cores and 1+1D or 2D chemical models of mature T Tauri and Herbig Ae/Be disks. One of the key questions is whether the chemical composition of such disks is mainly a result of chemical processing during the collapse or whether it is determined by in situ processing after the disk has formed.

As reviewed by di Francesco et al. (2007) and Bergin & Tafalla (2007), the chemistry of pre-stellar cores is well understood. Because of the low temperatures and the moderately high densities, a lot of molecules are observed to be depleted from the gas by freezing out onto the cold dust grains. The main ice constituent is H_2O, showing abundances of $\sim 10^{-4}$ relative to H_2 (Tielens et al. 1991, van Dishoeck 2004). Other abundant ices are CO_2 (30–35% of H_2O; Pontoppidan et al. 2008b) and CO (5–100% of H_2O; Jørgensen et al. 2005, Pontoppidan 2006). Correspondingly, the observed gas-phase abundances of H_2O, CO and CO_2 in pre-stellar cores are low (Snell et al. 2000, Ashby et al. 2000, Bergin

& Snell 2002, Bacmann et al. 2002). Nitrogen-bearing species like N_2 and NH_3 are generally less depleted than carbon- and oxygen-bearing ones (Rawlings et al. 1992, Tafalla et al. 2002, 2004), probably because they require a longer time to be formed in the gas and therefore have not yet had a chance to freeze out (di Francesco et al. 2007). The observed depletion factors are well reproduced with 1D chemical models (Bergin & Langer 1997, Lee et al. 2004).

The collapse phase is initially characterised by a gradual warm-up of the material, resulting in the evaporation of the ice species according to their respective binding energies (van Dishoeck et al. 1993, van Dishoeck & Blake 1998, Boogert et al. 2000, van der Tak et al. 2000a, Aikawa et al. 2001, Jørgensen et al. 2002, 2004, 2005, Jørgensen 2004). The higher temperatures also drive a rich chemistry, especially if it gets warm enough to evaporate H_2O and organic species like CH_3OH and $HCOOCH_3$ (Blake et al. 1987, Millar et al. 1991, Charnley et al. 1992). Going back to the late 1970s, the chemical evolution during the collapse phase has been studied with purely spherical models (Gerola & Glassgold 1978, Leung et al. 1984, Ceccarelli et al. 1996, Rodgers & Charnley 2003, Doty et al. 2004, Lee et al. 2004, Garrod & Herbst 2006, Aikawa et al. 2008, Garrod et al. 2008). They are successful at explaining the observed abundances at scales of several thousand AU, where the envelope is still close to spherically symmetric, but they cannot make the transition from the 1D spherically symmetric envelope to the 2D axisymmetric circumstellar disk.

Recently, van Weeren et al. (2009) followed the chemical evolution within the framework of a 2D hydrodynamical simulation and obtained a reasonable match with observations. However, their primary focus was still on the envelope, not on the disk. Nevertheless, they showed how important it is to treat the chemical evolution during low-mass star formation as more than a simple 1D process.

Once the phase of active accretion from the envelope comes to an end, the circumstellar disk settles into a comparatively static situation (Bergin et al. 2007, Dullemond et al. 2007a). Observationally, we are now in the T Tauri and Herbig Ae/Be stages, and some simple molecules have been detected in these objects (Dutrey et al. 1997, Kastner et al. 1997, Qi et al. 2003, Thi et al. 2004, Lahuis et al. 2006). They have also received a lot of attention with 2D models, showing for example that disks can be divided vertically into three chemical layers: a cold zone near the midplane, a warm molecular layer at intermediate altitudes, and a photon-dominated region at the surface (Aikawa et al. 1996, 1997, 2002, 2008, Aikawa & Herbst 1999, 2001, Willacy & Langer 2000, van Zadelhoff et al. 2003, Rodgers & Charnley 2003, Jonkheid et al. 2004, Semenov et al. 2006, Woitke et al. 2009). However, as noted above, the chemical connection between the early 1D stages of low-mass star formation and the 2D circumstellar disks at later stages remains an unsolved puzzle.

This chapter aims to provide the first steps towards solving this puzzle by following the chemical evolution all the way from a pre-stellar cloud core to a circumstellar disk in two spatial dimensions. The physical and chemical models are described in Sects. 3.2 and 3.3. We briefly discuss the chemistry during the pre-collapse phase in Sect. 3.4 before turning to the collapse itself in Sect. 3.5. There, we first follow the chemistry in detail along a trajectory terminating at one particular position in the disk, and then

generalise those results to material ending up at other positions. In Sect. 3.6, we compare the abundances resulting from the collapse to in situ processing in a static disk. Finally, we discuss some caveats and the implications of our results for the origin of comets in Sect. 3.7. Conclusions are drawn in Sect. 3.8.

3.2 Collapse model

3.2.1 Step-wise summary

Our semi-analytical collapse model is described in detail in Chapter 2; it consists of several steps, summarised in Fig. 3.1. We start with a singular isothermal sphere characterised by a total mass M_0, an effective sound speed c_s, and a uniform rotation rate Ω_0. As soon as the collapse starts, at $t = 0$, the rotation causes the infalling material to be deflected towards the equatorial midplane. This breaks the spherical symmetry, so we run the entire model as a two-dimensional axisymmetric system. The 2D density and velocity profiles follow the solutions of Shu (1977), Cassen & Moosman (1981) and Terebey et al. (1984) for an inside-out collapse with rotation. After the disk is first formed at the midplane, it evolves by ongoing accretion from the collapsing core and by viscous spreading to conserve angular momentum (Shakura & Sunyaev 1973, Lynden-Bell & Pringle 1974).

Taking the 2D density profiles from step 2, and adopting the appropriate size and luminosity for the protostar (Adams & Shu 1986, Young & Evans 2005), the next step consists of computing the dust temperature at a number of time steps. We do this with the radiative transfer code RADMC (Dullemond & Dominik 2004a), which takes a 2D axisymmetric density profile but follows photons in all three dimensions. The RADMC code also computes the full radiation spectrum at each point in the axisymmetric disk and remnant envelope, as required for the photon-driven reactions in our chemical network (Sects. 3.2.3 and 3.3.1). The gas temperature is set equal to the dust temperature throughout the disk and the envelope. This is a poor assumption in the surface of the disk and the

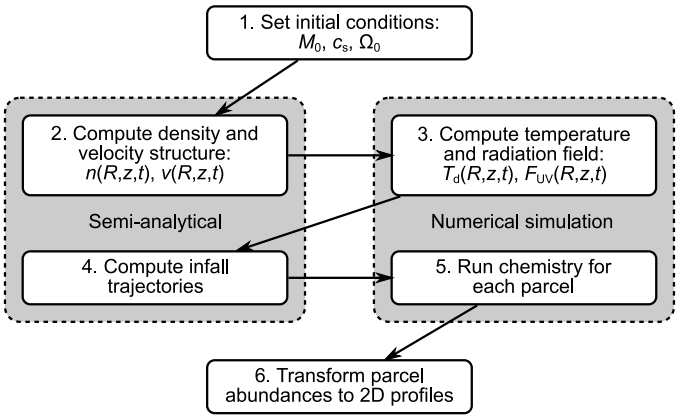

Figure 3.1 – Step-wise summary of our 2D axisymmetric collapse model. Steps 2 and 4 are semi-analytical, while steps 3 and 5 consist of detailed numerical simulations.

inner parts of the envelope (Kamp & Dullemond 2004, Jonkheid et al. 2004, Woitke et al. 2009), the consequences of which are addressed in Sect. 3.7.1.

Given the dynamical nature of the collapse, it is easiest to solve the chemistry in a Lagrangian frame. In Chapter 2, we populated the envelope with several thousand parcels at $t = 0$ and followed them in towards the disk and star. We now take an alternative approach where we define a regular grid of parcels at the end of the collapse and follow the parcels backwards in time to their position at $t = 0$. Since we are usually interested in the abundance profiles at the end of the collapse, when the disk is fully formed, it has many advantages to have a regular grid of parcels at that time rather than at the beginning. In either case, step 4 of the model produces a set of infall trajectories with densities, temperatures and UV intensities as a function of time and position. These data are required for the next step: solving the time-dependent chemistry for each individual parcel. Although the parcels are followed backwards in time to get their trajectories, we compute the chemistry in the normal forward direction. The last step of our model consists of transforming the abundances from the individual parcels back into 2D axisymmetric profiles at whatever time steps we are interested in.

In Chapter 2, the model was run for a grid of initial conditions. In the current chapter, the analysis is limited to our standard set of parameters: $M_0 = 1.0\ M_\odot$, $c_s = 0.26$ km s^{-1} and $\Omega_0 = 10^{-14}$ s^{-1}. Section 3.7.2 contains a brief discussion on how the results may change for other parameter values.

3.2.2 Differences with Chapter 2

The current version of the model contains several improvements over the version used in Chapter 2. Most importantly, it now correctly treats the problem of sub-Keplerian accretion onto a 2D disk. It has long been known that material falling onto the disk along an elliptic orbit has sub-Keplerian angular momentum, so it exerts a torque on the disk that results in an inward push. Several solutions are available (e.g., Cassen & Moosman 1981, Hueso & Guillot 2005), but these are not suitable for our 2D model. The ad-hoc solution from Chapter 2 provided the appropriate qualitative physical correction, namely increasing the inward radial velocity of the disk material, but it did not properly conserve angular momentum. We now use a new, fully consistent solution, derived directly from the equations for the conservation of mass and angular momentum. It is described in detail in Chapter 4, where it is also shown that it results in disks that are typically a factor of a few smaller than those obtained with the original model. The new disks are a few degrees colder in the inner part and warmer in the outer part, which may further affect the chemistry.

Other changes to the model include the definition of the disk-envelope boundary and the shape of the outflow cavity. In Chapter 2, the disk-envelope boundary was defined as the surface where the density of the infalling envelope material equals that of the disk. Instead, we now take the surface where the ram pressure of the infalling material equals the thermal pressure of the disk (see Chapter 4). This provides a more physically correct description of where material becomes part of the disk. The outflow cavity now has curved walls rather than straight ones, consistent with both observations and theoretical

predictions (Velusamy & Langer 1998, Cantó et al. 2008). The outflow wall is described by

$$z = (0.191\ \mathrm{AU}) \left(\frac{t}{t_{\mathrm{acc}}} \right)^{-3} \left(\frac{R}{\mathrm{AU}} \right)^{1.5} , \tag{3.1}$$

with R and z in spherical coordinates and $t_{\mathrm{acc}} = M_0/\dot{M}$ the time required for the entire envelope to accrete onto the star and disk. The t^{-3} dependence is chosen so that the outflow starts very narrow and becomes increasingly wide as the collapse proceeds. The full opening angle at t_{acc} is 33.6° at $z = 1000$ AU and 15.9° at $z = 10\,000$ AU.

3.2.3 Radiation field

Photodissociation and photoionisation by ultraviolet (UV) radiation are important processes in the hot inner core and in the surface layers of the disk. The temperature and luminosity of the protostar evolve as described in Chapter 2, so neither the strength nor the spectral shape of the radiation it emits are constant in time. In addition, the spectral shape changes as the radiation passes through the disk and remnant envelope. Hence, we cannot simply take the photorates from the interstellar medium and scale them according to the integrated UV flux at each spatial grid point.

The most accurate way to obtain the time- and location-dependent photorates is to multiply the cross section for each reaction by the UV field at each grid point. The latter can be computed from 2D radiative transfer at high spectral resolution. As this is too computationally demanding, several approximations have to be made. First of all, we assume the wavelength-dependent attenuation of the radiation field by the dust in the disk and envelope can be represented by a single factor γ for each reaction. The rate coefficient for a given photoreaction at spatial coordinates r and θ and at time t can then be expressed as

$$k_{\mathrm{ph}}(r, \theta, t) = k^*_{\mathrm{ph}} \left(\frac{r}{R_*} \right)^{-2} e^{-\gamma A_{\mathrm{V}}} , \tag{3.2}$$

with A_{V} the visual extinction towards that point. The unshielded rate coefficient is calculated at the stellar surface (k^*_{ph}) by multiplying the cross section of the reaction by the blackbody flux at the effective temperature of the protostar. The term $(r/R_*)^{-2}$ accounts for the geometrical dilution of the radiation from the star across a distance r. The factor γ is discussed in Sect. 3.3.1.

In order to apply Eq. (3.2), we need the extinction towards each point. In a 1D model, this can simply be done by integrating the total hydrogen number density from the star to a point r and converting the resulting column density to a visual extinction. This approach has been extended to 2D circumstellar disk models by dividing the disk into annuli, each irradiated only from the top and bottom (e.g., Aikawa & Herbst 1999, Jonkheid et al. 2004). Such a 1+1D method is poorly suited to our model, which always has infalling envelope material right above and below the disk. Instead, we compute an average UV flux for each spatial grid point at a number of time steps and compare it to the flux that would be obtained in the case of zero attenuation. The difference gives us an effective extinction for each point.

Table 3.1 – Elemental abundances: $x(X) = n(X)/n_{\rm H}$.

Species	Abundance	Species	Abundance	Species	Abundance
H_2	5.00(-1)	Na	2.25(-9)	Cl	1.00(-9)
He	9.75(-2)	Mg	1.09(-8)	Ar	3.80(-8)
C	7.86(-5)	Al	3.10(-8)	Ca	2.20(-8)
N	2.47(-5)	Si	2.74(-9)	Cr	4.90(-9)
O	1.80(-4)	P	2.16(-10)	Fe	2.74(-9)
Ne	1.40(-6)	S	9.14(-8)	Ni	1.80(-8)

The first step in this procedure is to run the Monte Carlo radiative transfer package RADMC (Dullemond & Dominik 2004a) at a low spectral resolution of one frequency point per eV. The large number of photons propagated through the grid (typically 10^5) ensures that we get a statistical sampling of the possible trajectories leading to each point. The specific UV fluxes thus obtained for a point (r, θ, t) are integrated from 6 to 13.6 eV to get the average flux ($F_{\rm UV}$). This flux is lower than that at the stellar surface because of geometrical dilution and attenuation by dust. Denoting the flux at the stellar surface as $F^*_{\rm UV}$, we can express the effects of dilution and attenuation as

$$F_{\rm UV}(r,\theta) = F^0_{\rm UV} e^{-\tau_{\rm UV,eff}} = F^*_{\rm UV} \left(\frac{r}{R_*}\right)^{-2} e^{-\tau_{\rm UV,eff}} . \tag{3.3}$$

The effective UV extinction, $\tau_{\rm UV,eff}$, is converted to the visual extinction $A_{\rm V}$ through the standard relationship $A_{\rm V} = \tau_{\rm UV,eff}/3.02$. The unattenuated UV flux, $F^0_{\rm UV}$, can also be expressed as a scaling factor relative to the average flux in the interstellar medium (ISM): $\chi = F^0_{\rm UV}/F_{\rm ISM}$, with $F_{\rm ISM} = 8 \times 10^7$ cm^{-2} s^{-1} (Draine 1978).

3.3 Chemical network

The basis of our chemical network is the UMIST06 database (Woodall et al. 2007) as modified by Bruderer et al. (2009), except that we do not include X-ray chemistry. The cosmic-ray ionisation rate of H_2 is set to 5×10^{-17} s^{-1} (van der Tak et al. 2000b, Doty et al. 2004, Dalgarno 2006). The network contains 162 neutral species, 251 cations and six anions, built up out of 18 elements. We take a fully atomic composition as the starting point, except that hydrogen starts as H_2. Elemental abundances are adopted from Aikawa et al. (2008), with additional values from Bruderer et al. (2009). The latter are reduced by a factor of 100 from the original undepleted values to account for the incorporation of these heavy elements into the dust grains. Table 3.1 lists the elemental abundances relative to the total hydrogen nucleus density: $n_{\rm H} = n({\rm H}) + 2n(H_2)$.

In order to set the chemical composition at the onset of collapse ($t = 0$), we evolve the initially atomic gas for a period of 1 Myr at $n_{\rm H} = 8 \times 10^4$ cm^{-3} and $T_{\rm g} = T_{\rm d} = 10$ K. The extinction during this pre-collapse phase is set to 100 mag to disable all photoprocesses, except for a minor contribution from cosmic-ray–induced photons. The resulting solid

and gas-phase abundances are consistent with those observed in pre-stellar cores (e.g., Bergin et al. 2000, di Francesco et al. 2007), and we take them as the initial condition for the collapse phase for all infalling parcels. In the remainder of this chapter, $t = 0$ always refers to the onset of collapse, following the 1 Myr pre-collapse phase here described.

3.3.1 Photodissociation and photoionisation

Photodissociation and photoionisation by UV radiation are important processes in the inner disk and inner envelope. Their rates are given by Eq. (3.2) using the extinction from Eq. (3.3). The extinction factor γ from Eq. (3.2) depends on the spectral shape of the radiation field, but it is not feasible to include this dependence in detail. Instead, we use the molecule-specific values tabulated for a 4000 K blackbody by van Dishoeck et al. (2006). The unshielded rates at the stellar surface ($k^*_{\rm ph}$) are calculated with the cross sections from our freely available database, compiled from Lee (1984), van Dishoeck (1988), Roberge et al. (1991), Huebner et al. (1992), van Dishoeck et al. (2006) and van Hemert & van Dishoeck (2008).[1] The final output of this procedure consists of a 3D array (time and two spatial coordinates) with rate coefficients for each photoreaction. When computing the infall trajectories for individual parcels (step 4 in Fig. 3.1), we perform a linear interpolation to get the rate coefficients at all points along each trajectory.

The photodissociation of H_2 and CO requires some special treatment. Both processes occur exclusively through discrete absorption lines, so self-shielding plays an important role. The amount of shielding for H_2 is a function of the H_2 column density; for CO, it is a function of both the CO and the H_2 column density, because some CO lines are shielded by H_2 lines. The effective UV extinction from Eq. (3.3) can be converted to a total hydrogen column density through $A_{\rm V} = \tau_{\rm UV,eff}/3.02$ and $N_{\rm H} = 1.59{\times}10^{21} A_{\rm V}$ cm^{-2} (Diplas & Savage 1994). Assuming that most hydrogen along each photon path is in molecular form, we simply set $N(H_2) = 0.5 N_{\rm H}$ to get the effective H_2 column density towards each spatial grid point. Equation (37) from Draine & Bertoldi (1996) then gives the amount of self-shielding for H_2. The unshielded dissociation rate is computed according to the one-line approximation from van Dishoeck (1987), scaled so that the rate is 4.5×10^{-11} s^{-1} in the standard Draine (1978) field. For CO, we use the new shielding functions and cross sections from Chapter 5. Effective CO column densities are derived from the H_2 column densities by assuming an average $N(CO)/N(H_2)$ ratio of 10^{-5}. Since both H_2 and CO require absorption of photons shortwards of 1100 Å, their dissociation rates are greatly reduced at $T_* \approx 4000$ K compared with the Draine field (see also van Zadelhoff et al. 2003). During the collapse, this results in a zone where molecules like H_2O and CH_4 are photodissociated, while H_2 and CO remain intact (Sect. 3.5.1).

3.3.2 Gas-grain interactions

We allow all neutral species other than H, H_2 and the three noble gases to freeze out onto the dust according to Charnley et al. (2001). In cold, dense environments – such as our

[1] http://www.strw.leidenuniv.nl/~ewine/photo

model cores before the onset of collapse – observations show H_2O, CO and CO_2 to be the most abundant ices (Gibb et al. 2004, Boogert et al. 2008). Of these three, H_2O and CO_2 are mixed together, but most CO is found to reside in a separate layer (Pontoppidan et al. 2003, 2008b). As the temperature rises during the collapse, the ices evaporate according to their binding energy. However, the presence of non-volatile species like H_2O prevents the more volatile species like CO and CO_2 from evaporating entirely: some CO and CO_2 gets trapped in the H_2O ice (Sandford & Allamandola 1988, Hasegawa & Herbst 1993, Collings et al. 2004). In Chapter 2, we showed that this is required to explain the presence of CO in solar-system comets.

Incorporating ice trapping in a chemical network is a non-trivial task. The approach of Viti et al. (2004) was primarily designed to reproduce the temperature-programmed desorption (TPD) experiments from Collings et al. (2004). It works for astrophysical models where the temperature is increasing monotonically, but as shown in Chapter 2, the infalling material in our collapse model goes through periods of decreasing temperature as well. We could still apply the Viti et al. method to a "network" consisting of only CO and H_2O (Chapter 2), but applying it to the full network currently used consistently leads to numerical instabilities. In addition, recent experiments by Fayolle et al. (in prep.) show that the amount of trapping depends on the ice thickness and the volatile-to-H_2O mixing ratio. Collings et al. performed all their experiments at the same thickness and the same mixing ratio, so the amount of trapping in the model of Viti et al. is independent of these properties.

We ignore trapping for now and treat desorption of all species according to the zeroth-order rate equation

$$R_{\mathrm{thdes}}(X) = 4\pi a_{\mathrm{gr}}^2 n_{\mathrm{gr}} f(X) \nu(X) \exp\left[-\frac{E_{\mathrm{b}}(X)}{kT_{\mathrm{d}}}\right], \tag{3.4}$$

where T_{d} is the dust temperature, $a_{\mathrm{gr}} = 0.1\ \mu$m the typical grain radius, and $n_{\mathrm{gr}} = 10^{-12} n_{\mathrm{H}}$ the grain number density. The canonical pre-exponential factor, ν, for *first*-order desorption is 2×10^{12} s^{-1} (Sandford & Allamandola 1993). We multiply this by the number of binding sites per unit grain surface (8×10^{14} cm^{-2} for our 0.1 μm grains, assuming 10^6 binding sites per grain) to get a *zeroth*-order pre-exponential factor of 2×10^{27} cm^{-2} s^{-1}. This value is used for all ice species, with the exception of the four listed in Table 3.2. The binding energies of species other than those four are set to the values tabulated by Sandford & Allamandola (1993) and Aikawa et al. (1997). Species for which the binding energy is unknown are assigned the binding energy *and* the pre-exponential factor of H_2O. The dimensionless factor f in Eq. (3.4) ensures that each species desorbs according to its abundance in the ice, and changes the overall desorption behaviour from zeroth to first order when there is less than one monolayer of ice:

$$f(X) = \frac{n_{\mathrm{s}}(X)}{\max(n_{\mathrm{ice}}, N_{\mathrm{b}} n_{\mathrm{gr}})}, \tag{3.5}$$

with $N_{\mathrm{b}} = 10^6$ the typical number of binding sites per grain and n_{ice} the total number density (per unit volume of cloud or disk) of all ice species combined. We briefly discuss in Sect. 3.7.1 how our results might change if we include trapping.

Table 3.2 – Pre-exponential factors and binding energies for selected species in our network.

Species	ν (cm^{-2} s^{-1})	E_b/k (K)	Reference
H_2O	1×10^{30}	5773	Fraser et al. (2001)
CO	7×10^{26}	855	Bisschop et al. (2006)
N_2	8×10^{25}	800	Bisschop et al. (2006)
O_2	7×10^{26}	912	Acharyya et al. (2007)

In addition to thermal desorption, our model includes desorption induced by UV photons. Laboratory experiments on the photodesorption of H_2O, CO and CO_2 all produce a yield of $Y \approx 10^{-3}$ molecules per grain per incident UV photon (Westley et al. 1995a,b, Öberg et al. 2007, 2009b), while the yield for N_2 is an order of magnitude lower (Öberg et al. 2009c). Classical dynamics calculations predict a somewhat lower yield of 4×10^{-4} for H_2O (Andersson et al. 2006, Andersson & van Dishoeck 2008). The yields depend to some extent on properties like the dust temperature and the ice thickness, but this has little effect on chemical models (Öberg et al. 2009b). Hence, we take a constant yield of 10^{-3} for H_2O, CO and CO_2, and of 10^{-4} for N_2. For all other ice species in our network, whose photodesorption yields have not yet been determined experimentally or theoretically, we also take a yield of 10^{-3}. The photodesorption rate then becomes

$$R_\mathrm{phdes}(X) = \pi a_\mathrm{gr}^2 n_\mathrm{gr} f(X) Y(X) F_\mathrm{UV}^0 e^{-\tau_\mathrm{UV,eff}} , \tag{3.6}$$

with f the same factor as for thermal desorption. The unattenuated UV flux (F_UV^0) and the effective UV extinction ($\tau_\mathrm{UV,eff}$) follow from Eq. (3.3). Photodesorption occurs even in strongly shielded regions because of cosmic-ray–induced photons. We incorporate this effect by setting a lower limit of 10^4 cm^{-2} s^{-1} to F_UV^0 (Shen et al. 2004).

The chemical reactions in our model are not entirely limited to the gas phase. As usual, the network includes the grain-surface formation of H_2 (Black & van Dishoeck 1987). Inspired by Bergin et al. (2000) and Hollenbach et al. (2009), it also includes the hydrogenation of C to CH_4, N to NH_3, O to H_2O, and S to H_2S. The hydrogenation is done one H atom at a time and is always in competition with thermal and photon-induced desorption. The formation of CH_4, NH_3, H_2O and H_2S does not have to start with the respective atom freezing out. For instance, CH freezing out from the gas is also subject to hydrogenation on the grain surface. The rate of each hydrogenation step is taken to be the adsorption rate of H from the gas multiplied by the probability that the H atom finds the atom or molecule X to hydrogenate:

$$R_\mathrm{hydro}(X) = \pi a_\mathrm{gr}^2 n_\mathrm{gr} n(\mathrm{H}) f'(X) \sqrt{\frac{8kT_\mathrm{g}}{\pi m_\mathrm{p}}} \tag{3.7}$$

with T_g the gas temperature. The factor f' serves a similar purpose as the factor f in Eqs. (3.4) and (3.6). Since the hydrogenation is assumed to be near-instantaneous as soon as the H atom meets X before X desorbs, X is assumed to reside always near the top layer of the ice. Hence, we are not interested in the abundance of solid X relative to the

total amount of ice (as in f), but in its abundance relative to the other species that can be hydrogenated:

$$f'(X) = \frac{n_\mathrm{s}(X)}{\max(n_\mathrm{hydro}, N_\mathrm{b} n_\mathrm{gr})}\,, \tag{3.8}$$

with n_hydro the sum of the solid abundances of the eleven species X: C, CH, CH_2, CH_3, N, NH, NH_2, O, OH, S and SH. The main effect of this hydrogenation scheme is to build up an ice mixture of simple saturated molecules during the pre-collapse phase, as is found observationally (Tielens et al. 1991, Gibb et al. 2004, Tafalla et al. 2004, van Dishoeck 2004, Öberg et al. 2008).

Grain-surface hydrogenation is known to occur for more species than just the eleven included here. For example, CO can be hydrogenated to form H_2CO and CH_3OH (Watanabe & Kouchi 2002, Fuchs et al. 2009). Grains also play an important role in the formation of more complex species (Garrod & Herbst 2006, Garrod et al. 2008, Öberg et al. 2009a). However, none of these reactions can be implemented as easily as the hydrogenation of C, N, O and S. In addition, the main focus of this chapter is on simple molecules whose abundances can be well explained with conventional gas-phase chemistry. Therefore, we are safe in ignoring the more complex grain-surface reactions.

3.4 Results from the pre-collapse phase

This section, together with the next two, contains the results from the gas-phase chemistry in our collapse model. First we briefly discuss what happens during the pre-collapse phase. The chemistry during the collapse is analysed in detail for one particular parcel in Sect. 3.5.1 and then generalised to others in Sect. 3.5.2. Finally, we compare the collapse chemistry to a static disk model in Sect. 3.6. The results in this section are all consistent with available observational constraints on pre-stellar cores (e.g., Bergin et al. 2000, di Francesco et al. 2007).

During the 1.0 Myr pre-collapse phase, the initially atomic oxygen gradually freezes out and is hydrogenated to H_2O ice. Meanwhile, H_2 is ionised by cosmic rays and the resulting H_2^+ reacts with H_2 to give H_3^+. This sets off the following chain of oxygen chemistry:

$$\mathrm{O} + \mathrm{H_3^+} \rightarrow \mathrm{OH^+} + \mathrm{H_2}\,, \tag{3.9}$$

$$\mathrm{OH^+} + \mathrm{H_2} \rightarrow \mathrm{H_2O^+} + \mathrm{H}\,, \tag{3.10}$$

$$\mathrm{H_2O^+} + \mathrm{H_2} \rightarrow \mathrm{H_3O^+} + \mathrm{H}\,, \tag{3.11}$$

$$\mathrm{H_3O^+} + \mathrm{e^-} \rightarrow \mathrm{OH} + \mathrm{H_2}/2\mathrm{H}\,, \tag{3.12}$$

$$\mathrm{OH} + \mathrm{O} \rightarrow \mathrm{O_2} + \mathrm{H}\,. \tag{3.13}$$

The O_2 thus produced freezes out for the most part. At the onset of collapse, the four major oxygen reservoirs are H_2O ice (44%), CO ice (34%), O_2 ice (16%) and NO ice (3%).

The oxygen chemistry is tied closely to the carbon chemistry through CO. It is initially formed in the gas phase from CH_2, which in turn is formed from atomic C:

$$C + H_2 \rightarrow CH_2\,, \tag{3.14}$$

$$CH_2 + O \rightarrow CO + 2H\,. \tag{3.15}$$

Another early pathway from C to CO is powered by H_3^+ and goes through an HCO^+ intermediate:

$$C + H_3^+ \rightarrow CH^+ + H_2\,, \tag{3.16}$$

$$CH^+ + H_2 \rightarrow CH_2^+ + H\,, \tag{3.17}$$

$$CH_2^+ + H_2 \rightarrow CH_3^+ + H\,, \tag{3.18}$$

$$CH_3^+ + O \rightarrow HCO^+ + H_2\,, \tag{3.19}$$

$$HCO^+ + C \rightarrow CO + CH^+\,. \tag{3.20}$$

The formation of CO through these two pathways accounts for most of the pre-collapse processing of carbon: at $t = 0$, 82% of all carbon has been converted into CO, of which 97% has frozen out onto the grains. Most of the remaining carbon is present as CH_4 ice (14% of all C), formed from the rapid grain-surface hydrogenation of atomic C.

The initial nitrogen chemistry consists mostly of converting atomic N into NH_3, N_2 and NO. The first of these is formed on the grains after freeze-out of N, in the same way that H_2O and CH_4 are formed from adsorbed O and C. We find two pathways leading to N_2. The first one starts with the cosmic-ray dissociation of H_2:

$$H_2 + \zeta \rightarrow H^+ + H^-\,, \tag{3.21}$$

$$N + H^- \rightarrow NH + e^-\,, \tag{3.22}$$

$$NH + N \rightarrow N_2 + H\,. \tag{3.23}$$

The other pathway couples the nitrogen chemistry to the carbon chemistry. It starts with Reactions (3.16)–(3.18) to form CH_3^+, followed by

$$CH_3^+ + e^- \rightarrow CH + H_2/2H\,, \tag{3.24}$$

$$CH + N \rightarrow CN + H\,, \tag{3.25}$$

$$CN + N \rightarrow N_2 + C\,. \tag{3.26}$$

The nitrogen chemistry is also tied to the oxygen chemistry, forming NO out of N and OH:

$$N + OH \rightarrow NO + H\,, \tag{3.27}$$

with OH formed by Reaction (3.12). Nearly all of the N_2 and NO formed during the pre-collapse phase freezes out. At $t = 0$, solid N_2, solid NH_3 and solid NO account for 41, 32 and 22% of all nitrogen.

3.5 Results from the collapse phase

3.5.1 One single parcel

The collapse-phase chemistry is run for the standard set of model parameters from Chapter 2: $M_0 = 1.0\ M_\odot$, $c_s = 0.26$ km s^{-1} and $\Omega_0 = 10^{-14}$ s^{-1}. We first discuss the chemistry in detail for one particular infalling parcel of material. It starts near the edge of the cloud core, at 6710 AU from the center and 48.8° degrees from the z axis. Its trajectory terminates at $t = t_{\rm acc}$ at $R = 6.3$ AU and $z = 2.4$ AU, about 0.2 AU below the surface of the disk. The physical conditions encountered along the trajectory (χ, $n_{\rm H}$, $T_{\rm d}$ and $A_{\rm V}$) are plotted in Fig. 3.2. This figure also shows the abundances of the main oxygen-, carbon- and nitrogen-bearing species. The right four panels are regular plots as function of R: the coordinate along the midplane. The infall velocity of the parcel increases as it gets closer to the star, so the physical conditions and chemical abundances change ever more rapidly at later times. Hence, the left panel of each row is plotted as a function of $t_{\rm acc} - t$: the time before the end of the collapse phase. In each individual panel, the parcel essentially moves from right to left.

A schematic overview of the parcel's chemical evolution is presented in Fig. 3.3. It shows the infall trajectory of the parcel and the abundances of several species at four points along the trajectory. The physical conditions and the key reactions controlling those abundances are also listed. Most abundance changes for individual species are related to one specific chemical event, such as the evaporation of CO or the photodissociation of H_2O. The remainder of this subsection discusses the abundance profiles from Fig. 3.2 and explains them in the context of Fig. 3.3.

3.5.1.1 Oxygen chemistry

At the onset of collapse ($t = 0$), the main oxygen reservoir is solid H_2O at an abundance of 8×10^{-5} relative to $n_{\rm H}$. The abundance remains constant until the parcel gets to point C in Fig. 3.3, where the temperature is high enough for the H_2O ice to evaporate. The parcel is now located close to the outflow wall, so the stellar UV field is only weakly attenuated ($A_{\rm V} = 0.7$ mag). Hence, the evaporating H_2O is immediately photodissociated into H and OH, which in turn is dissociated into O and a second H atom. At $R = 17$ AU (23 AU inside of point C), the dust temperature is 150 K and all solid H_2O is gone. Moving in further, the parcel enters the surface layers of the disk and is quickly shielded from the stellar radiation ($A_{\rm V} = 10$–20 mag). The temperature decreases at the same time to 114 K, allowing some H_2O ice to reform. The final abundance at $t_{\rm acc}$ (point D) is 4×10^{-8}.

The dissociative recombination of H_3O^+ (formed by Reactions (3.9)–(3.11)) initially maintains H_2O in the gas at an abundance of 7×10^{-8}. Following the sharp increase in the overall gas density at $t = 2.1 \times 10^5$ yr (Fig. 3.2), the freeze-out rate increases and the gas-phase H_2O abundance goes down to 3×10^{-10} at point A in Fig. 3.3. Moving on towards point B, the evaporation of O_2 from the grains enables a new H_2O formation route:

$$O_2 + C^+ \rightarrow CO + O^+ , \tag{3.28}$$

$$O^+ + H_2 \rightarrow OH^+ + H\,, \tag{3.29}$$

followed by Reactions (3.10) and (3.11) to give H_3O^+, which recombines with an electron to give H_2O. The H_2O abundance thus increases to 3×10^{-9} at $R = 300$ AU. Farther in, at point C, solid H_2O comes off the grains as described above. However, photodissociation keeps the gas-phase abundance from growing higher than $\sim10^{-7}$. Once all H_2O ice is gone at $R = 17$ AU, the gas-phase abundance can no longer be sustained at 10^{-7} and it drops to 3×10^{-12}. Some H_2O is eventually reformed as the parcel gets into the disk and is shielded from the stellar radiation, producing a final abundance of 2×10^{-11} relative to n_H.

Another main oxygen reservoir at $t = 0$ is solid O_2, with an abundance of 1×10^{-5}. The corresponding gas-phase abundance is 4×10^{-7}. O_2 gradually continues to freeze out until it reaches a minimum gas-phase abundance of 3×10^{-10} just inside of point A. The temperature at that time is 19 K, enough for O_2 to slowly start evaporating thermally. The gas-phase abundance is up by a factor of ten by the time the dust temperature reaches 23 K, about halfway between points A and B. The evaporation is 99% complete as the parcel reaches $R = 460$ AU, about 140 AU inside of point B. The gas-phase abundance remains stable at 1×10^{-5} for the next few hundred years. Then, as the parcel gets closer to the outflow wall and into a region of lower extinction, the photodissociation of O_2 sets in and its abundance decreases to 2×10^{-8} at point C. The evaporation and photodissociation of H_2O at that point enhances the abundances of OH and O, which react with each other to replenish some O_2. As soon as all the H_2O ice is gone, this O_2 production channel quickly disappears and the O_2 abundance drops to 1×10^{-11}. Finally, when the parcel enters the top of the disk, O_2 is no longer photodissociated and its abundance goes back up to 4×10^{-8} at point D.

The abundance of gas-phase OH starts at 3×10^{-7}. Its main formation pathway is initially the dissociative recombination of H_3O^+ (Reaction (3.12)), and its main destructors are O, N and H_3^+. The increase in total density at 2.1×10^5 yr speeds up the destruction reactions, and the OH abundance drops to 3×10^{-10} at point B. The evaporation of solid OH then briefly increases the gas-phase abundance to 1×10^{-8}. When all of the OH has evaporated at $R = 300$ AU, the gas-phase abundance goes down again to 5×10^{-10} over the next 150 AU. As the parcel continues towards and past point C, the OH abundance is boosted to a maximum of 1×10^{-6} by the photodissociation of H_2O. The high abundance lasts only briefly, however. As the last of the H_2O evaporates and gets photodissociated, OH can no longer be formed as efficiently, and it is itself photodissociated. At the end of the collapse, the OH abundance is $\sim10^{-14}$.

The fifth main oxygen-bearing species is atomic O itself. Its abundance is 7×10^{-7} at $t = 0$ and 1×10^{-4} at $t = t_{acc}$, accounting for respectively 0.4 and 56% of the total amount of free oxygen. Starting from $t = 0$, the O abundance remains constant during the first 2.0×10^5 yr of the collapse phase. The increasing overall density then speeds up the reactions with OH (forming O_2) and H_3^+ (forming OH^+), as well as the desorption onto the grains, and the O abundance decreases to a minimum of 2×10^{-8} just before point A. The abundance goes back up thanks to the evaporation of CO and, at point B, of O_2 and

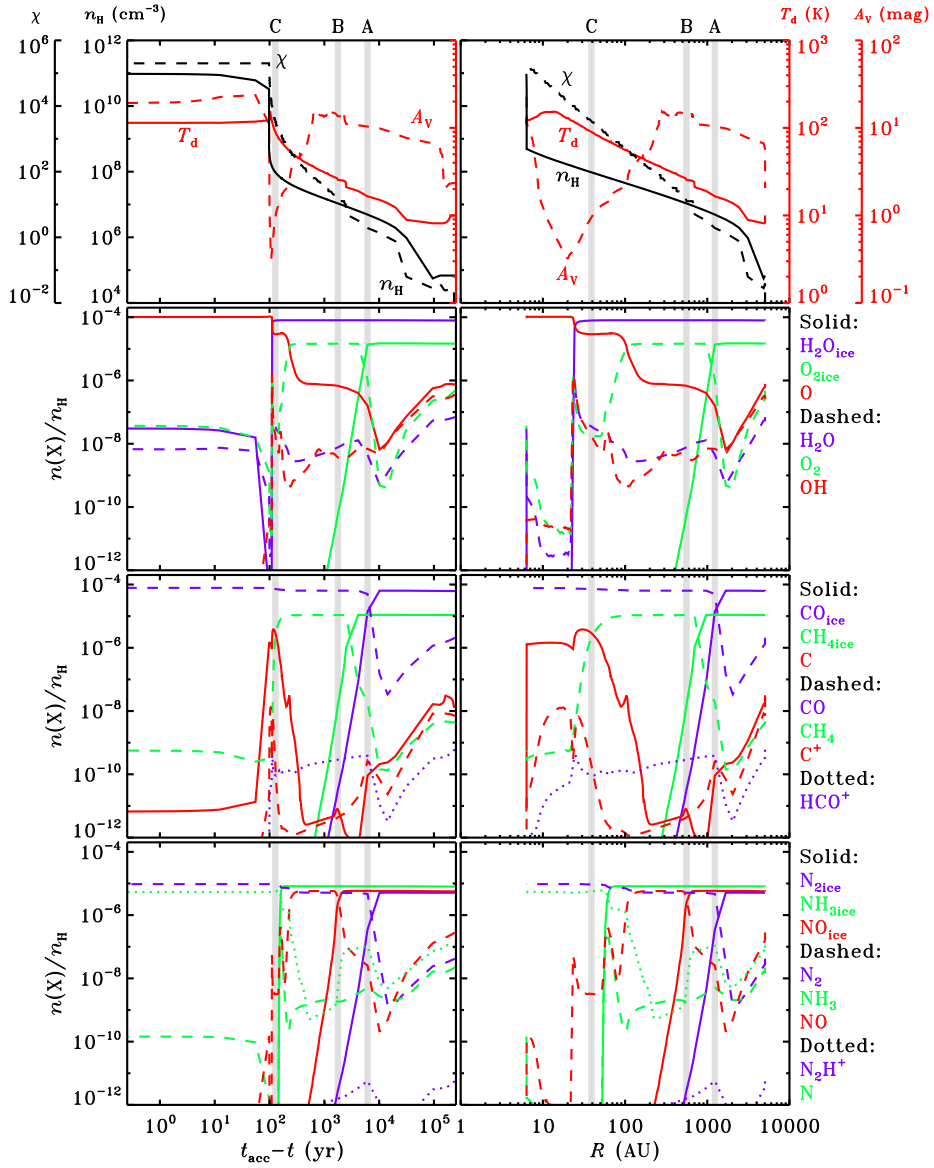

Figure 3.2 – Physical conditions (χ, n_H, T_d and A_V) and abundances of the main oxygen-, carbon- and nitrogen-bearing species for the single parcel from Sect. 3.5.1, as function of time before the end of the collapse (left) and as function of horizontal position (right). The grey bars correspond to the points A, B and C from Fig. 3.3. Note that in each panel, the parcel moves from right to left.

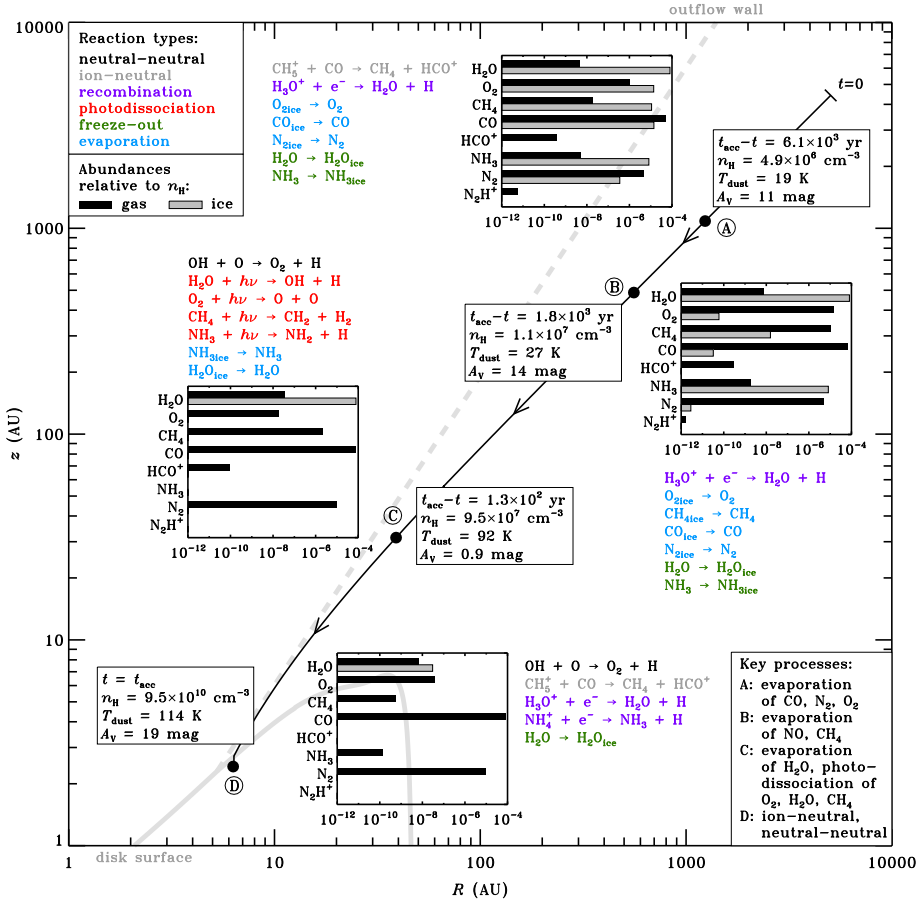

Figure 3.3 – Overview of the chemistry along the infall trajectory of the single parcel from Sect. 3.5.1. The solid and dashed grey lines denote the surface of the disk and the outflow wall, both at $t = t_{acc} = 2.52 \times 10^5$ yr. Physical conditions, abundances (black bars: gas; grey bars: ice) and key reactions are indicated at four points (A, B, C and D) along the trajectory. The key processes governing the overall chemistry at each point are listed in the bottom right. The type of each reaction is indicated by colour, as listed in the top left.

NO, with O formed from the following reactions:

$$\mathrm{CO + He^+ \rightarrow C^+ + O + He}\,, \tag{3.30}$$

$$\mathrm{NO + N \rightarrow N_2 + O}\,, \tag{3.31}$$

$$\mathrm{O_2 + CN \rightarrow OCN + O}\,. \tag{3.32}$$

Heading on towards point C, the photodissociation of O_2, NO and H_2O further drives up the amount of atomic O to the aforementioned final abundance of 1×10^{-4}.

3.5.1.2 Carbon chemistry

With solid and gas-phase abundances of 6×10^{-5} and 2×10^{-6} relative to $n_{\rm H}$, CO is the main form of free carbon at the onset of collapse. CO is a very stable molecule and its chemistry is straightforward. The freeze-out process started during the pre-collapse phase continues up to $t = 2.4 \times 10^5$ yr, a few thousand years prior to reaching point A in Fig. 3.3, where the dust temperature of 18 K results in CO evaporating again. As the parcel continues its inward journey and is heated up further, all solid CO rapidly disappears and the gas-phase abundance goes up to 6×10^{-5} at point B. During the remaining part of the infall trajectory, the other main carbon-bearing species (e.g., C, CH, CH_2, C_2 and HCO^+) are all largely converted into CO. At the end of the collapse (point D), 99.8% of the available carbon is locked up in CO. It also contains for 44% of the available oxygen.

The protonated form of CO, HCO^+, starts the collapse phase at an abundance of 6×10^{-10} relative to $n_{\rm H}$, or 3×10^{-4} relative to n(CO). It is in equilibrium with CO via the two reactions

$$\mathrm{CO} + \mathrm{H_3^+} \rightarrow \mathrm{HCO^+} + \mathrm{H_2}\,, \tag{3.33}$$

$$\mathrm{HCO^+} + \mathrm{e^-} \rightarrow \mathrm{CO} + \mathrm{H}\,. \tag{3.34}$$

It is possible to derive a simple analytical estimate of the HCO^+-CO abundance ratio. As shown by Lepp et al. (1987), the H_3^+ density does not depend strongly on the total gas density. We find $n(H_3^+) \approx 1 \times 10^{-4}$ cm^{-3} along the entire trajectory, except for the part outside point A, where most CO is frozen out and therefore unable to destroy H_3^+. If the cosmic-ray ionisation rate is changed from our current value of 5×10^{-17} s^{-1}, the H_3^+ density would change proportionally. The electron abundance is roughly constant at 3×10^{-8} relative to $n_{\rm H}$. Denoting the rate coefficients for Reactions (3.33) and (3.34) as $k_{\rm f}$ and $k_{\rm b}$, and assuming HCO^+ and CO to be in mutual equilibrium, we get

$$k_{\rm f} n(\mathrm{CO}) n(\mathrm{H_3^+}) \approx k_{\rm b} n(\mathrm{HCO^+}) n(\mathrm{e^-})\,. \tag{3.35}$$

Substituting $n(H_3^+) = 1 \times 10^{-4}$ cm^{-3}, $n(e^-) = 3 \times 10^{-8} n_{\rm H}$, $k_{\rm f} = 1.7 \times 10^{-9}$ cm^3 s^{-1} (Kim et al. 1975) and $k_{\rm b} = 2.4 \times 10^{-7} (T_{\rm g}/300\ {\rm K})^{-0.69}$ cm^3 s^{-1} (Mitchell 1990), this rearranges to

$$\frac{n(\mathrm{HCO^+})}{n(\mathrm{CO})} \approx 5 \times 10^{-4} \left(\frac{n_{\rm H}}{10^4\ {\rm cm^{-3}}} \right)^{-1} \left(\frac{T_{\rm g}}{30\ {\rm K}} \right)^{0.69}\,. \tag{3.36}$$

The overall density increases by six orders of magnitude along the entire trajectory, while the temperature changes only by one, so the HCO^+-CO abundance ratio should be roughly inversely proportional to the density. Our full chemical simulation confirms this relationship to within an order of magnitude throughout the collapse. However, the ratio comes out about a factor of ten larger than what is predicted by Eq. (3.36). The HCO^+ abundance reaches a final value at $t_{\rm acc}$ of 8×10^{-13} relative to $n_{\rm H}$, or 1×10^{-8} relative to n(CO).

The second most abundant carbon-bearing ice at the onset of collapse is CH_4, at 1×10^{-5} with respect to n_H. The gas-phase abundance of CH_4 begins at 4×10^{-9}, about a factor of 2500 lower. At point A, the evaporation of CO provides the first increase in $x(CH_4)$ through a chain of reactions starting with the formation of C^+ from CO. The successive hydrogenation of C^+ produces CH_5^+, which reacts with another CO molecule to form CH_4:

$$CO + He^+ \rightarrow C^+ + O + He\,, \tag{3.37}$$

$$C^+ + H_2 \rightarrow CH_2^+\,, \tag{3.38}$$

$$CH_2^+ + H_2 \rightarrow CH_3^+ + H\,, \tag{3.39}$$

$$CH_3^+ + H_2 \rightarrow CH_5^+\,, \tag{3.40}$$

$$CH_5^+ + CO \rightarrow CH_4 + HCO^+\,. \tag{3.41}$$

The CH_4 ice evaporates at point B, bringing the gas-phase abundance up to 1×10^{-5}. So far, the abundances of CH_4 and CO are well coupled. The link is broken when the parcel reaches point C, where CH_4 is photodissociated, but CO is not. This difference arises from the fact that CO can only be dissociated by photons shortwards of 1076 Å, while CH_4 can be dissociated out to 1450 Å (Chapter 5). The 5300 K blackbody spectrum emitted by the protostar at this time is not powerful enough at short wavelengths to cause significant photodissociation of CO. CH_4, on the other hand, is quickly destroyed. Its final abundance at point D is 6×10^{-10}.

Neutral and ionised carbon show the same trends in their abundance profiles, with the former always more abundant by a few per cent to a few orders of magnitude. Both start the collapse phase at $\sim 10^{-8}$ relative to n_H. The increase in total density at 2.1×10^5 yr speeds up the destruction reactions (mainly by OH and O_2 for C and by OH and H_2 for C^+), so the abundances go down to $x(C) = 4 \times 10^{-10}$ and $x(C^+) = 5 \times 10^{-11}$ just outside point A. This is where CO begins to evaporate, and as a result, the C and C^+ abundances increase again. As the parcel continues to fall in towards point B, the evaporation of O_2 and NO and the increasing total density cause a second drop in C and C^+. Once again, though, the drop is of a temporary nature. Moving on towards point C, the parcel gets exposed to the stellar UV field. The photodissociation of CH_4 leads – via intermediate CH, CH_2 or CH_3 – to neutral C, part of which is ionised to also increase the C^+ abundance. Finally, at point D, the photoprocesses no longer play a role, so the C and C^+ abundances go back down. Their final values relative to n_H are 7×10^{-12} and $\sim 10^{-14}$.

3.5.1.3 Nitrogen chemistry

The most common nitrogen-bearing species at $t = 0$ is solid N_2, with an abundance of 5×10^{-6}. The corresponding gas-phase abundance is 4×10^{-8}. The evolution of N_2 parallels that of CO, because they have similar binding energies and are both very stable molecules (Bisschop et al. 2006). N_2 continues to freeze out slowly until it gets near point A in Fig. 3.3, where the grain temperature of ~18 K causes all N_2 ice to evaporate. The

gas-phase N_2 remains intact along the rest of the infall trajectory and its final abundance is 1×10^{-5}, accounting for 77% of all nitrogen.

The parallels between CO and N_2 extend to their respective protonated forms, HCO^+ and N_2H^+. An approximate equilibrium exists between N_2 and N_2H^+ through the reactions

$$N_2 + H_3^+ \rightarrow N_2H^+ + H_2\,, \tag{3.42}$$

$$N_2H^+ + e^- \rightarrow N_2 + H\,. \tag{3.43}$$

The recombination of N_2H^+ also has a product channel of NH and N (Geppert et al. 2004), but this still results in N_2 being reformed through the additional reactions

$$NH + O \rightarrow NO + H\,, \tag{3.44}$$

$$NO + N \rightarrow N_2 + O\,, \tag{3.45}$$

$$NO + NH \rightarrow N_2 + O + H\,. \tag{3.46}$$

Assuming that the recombination of N_2H^+ eventually results in the formation of N_2 most of the time, we repeat the method outlined for the HCO^+-CO abundance ratio to derive the expected relationship

$$\frac{n(N_2H^+)}{n(N_2)} \approx 5 \times 10^{-4} \left(\frac{n_H}{10^4\ \mathrm{cm}^{-3}}\right)^{-1} \left(\frac{T_g}{30\ \mathrm{K}}\right)^{0.51}\,. \tag{3.47}$$

The results from the full chemical model show that within an order of magnitude, the N_2H^+-N_2 abundance ratio is indeed inversely proportional to the overall density and follows the prediction from Eq. (3.47). In the previous subsection, the ratio between HCO^+ and CO was also found to be roughly inversely proportional to the density (Eq. (3.36)). An important difference between N_2H^+ and HCO^+ arises from the reaction

$$N_2H^+ + CO \rightarrow N_2 + HCO^+\,, \tag{3.48}$$

which transforms some N_2H^+ into HCO^+ as soon as CO evaporates. This reaction is responsible for the drop in N_2H^+ right after point A.

The second largest nitrogen reservoir at the onset of collapse is NH_3, with solid and gas-phase abundances of 8×10^{-6} and 2×10^{-8}. The gas-phase abundance receives a short boost at point A due to the evaporation of N_2, followed by

$$N_2 + He^+ \rightarrow N^+ + N + He\,, \tag{3.49}$$

$$N^+ + H_2 \rightarrow NH^+ + H\,, \tag{3.50}$$

$$NH^+ + H_2 \rightarrow NH_2^+ + H\,, \tag{3.51}$$

$$NH_2^+ + H_2 \rightarrow NH_3^+ + H\,, \tag{3.52}$$

$$NH_3^+ + H_2 \rightarrow NH_4^+ + H\,, \tag{3.53}$$

$$NH_4^+ + e^- \rightarrow NH_3 + H\,. \tag{3.54}$$

The binding energy of NH_3 is intermediate to that of O_2 and H_2O, so it evaporates between points B and C. Like H_2O, NH_3 is photodissociated upon evaporation. As the last of the NH_3 ice leaves the grains at $R = 50$ AU (10 AU outside of point C), the gas-phase reservoir is no longer replenished and $x(NH_3)$ drops to $\sim 10^{-14}$. Some NH_3 is eventually reformed as the parcel gets into the disk, and the final abundance at point D is 1×10^{-10} relative to n_H.

With an abundance of 6×10^{-6}, solid NO is the third major initial nitrogen reservoir. Gaseous NO is a factor of twenty less abundant at $t = 0$: 3×10^{-7}. The NO gas is gradually destroyed prior to reaching point A by continued freeze-out and reactions with H^+ and H_3^+. It experiences a brief gain at point A from the evaporation of OH and its subsequent reaction with N to give NO and H. As the parcel continues to point B, the solid NO begins to evaporate and the gas-phase abundance rises to 6×10^{-6}. Photodissociation reactions then set in around $R = 100$ AU and the NO abundance goes back down to 6×10^{-9}. The evaporation and photodissociation of NH_3 cause a brief spike in the NO abundance through the reactions

$$NH_3 + h\nu \rightarrow NH_2 + H\,, \tag{3.55}$$

$$NH_2 + O \rightarrow HNO + H\,, \tag{3.56}$$

$$HNO + h\nu \rightarrow NO + H\,. \tag{3.57}$$

The evaporation of the last of the NH_3 ice at $R = 50$ AU eliminates this channel and the NO gas abundance decreases to 3×10^{-9} at point C. NO is now mainly sustained by the reaction between OH and N. As described above, the OH abundance drops sharply at $R = 17$ AU, and the NO abundance follows suit. The final abundance at point D is $\sim 10^{-14}$.

The last nitrogen-bearing species from Fig. 3.2 is atomic N itself. It starts at an abundance of 1×10^{-7} and slowly freezes out to an abundance of 2×10^{-8} just before reaching point A. At point A, N_2 evaporates and is partially converted to N_2H^+ by Reaction (3.42). The dissociative recombination of N_2H^+ mostly reforms N_2, but, as noted above, there is also a product channel of NH and N. The N abundance jumps back to 1×10^{-7} and remains nearly constant at that value until the parcel reaches point B, where NO evaporates and reacts with N to produce N_2 and O (Reaction (3.45)). This reduces x(N) to a minimum of 5×10^{-10} between points B and C. Moving in further, the parcel gets exposed to the stellar UV field, and NO and NH_3 are photodissociated to bring the N abundance to a final value of 5×10^{-6} relative to n_H. As such, it accounts for 22% of all nitrogen at the end of the collapse.

3.5.2 Other parcels

At the end of the collapse ($t = t_{acc}$), the parcel from Sect. 3.5.1 (hereafter called our reference parcel) is located at $R = 6.3$ AU and $z = 2.4$ AU, about 0.2 AU below the surface of the disk. As shown in Fig. 3.3, its trajectory passes close to the outflow wall, through a region of low extinction. This results in the photodissociation or photoionisation of

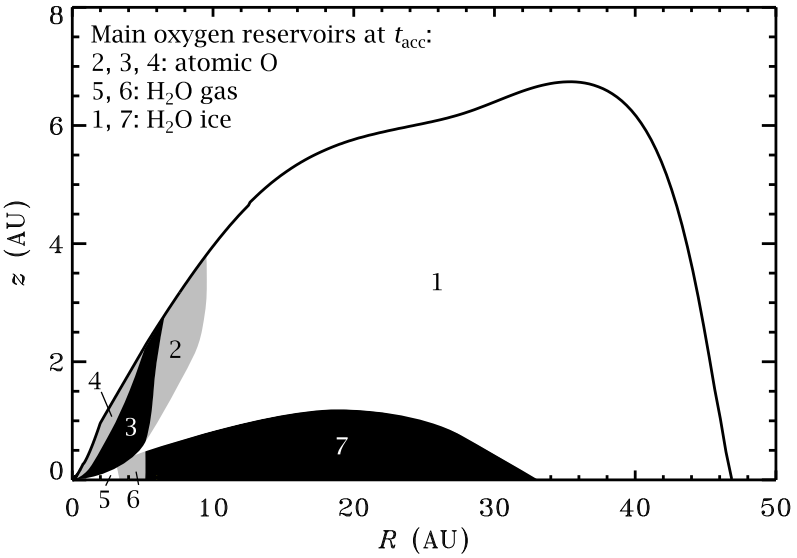

Figure 3.4 – Schematic view of the history of H_2O gas and ice throughout the disk. The main oxygen reservoir at t_{acc} is indicated for each zone; the histories are described in the text. Note the disproportionality of the R and z axes.

many species. At the same time, the parcel experiences dust temperatures of up to 150 K (Fig. 3.2), well above the evaporation temperature of H_2O and all other non-refractory species in our network. Material that ends up in other parts of the disk encounters different physical conditions during the collapse and therefore undergoes a different chemical evolution. This subsection shows how the absence or presence of some key chemical processes, related to certain physical conditions, affects the chemical history of the entire disk. Table 3.3 lists the abundances of selected species at four points in the disk at t_{acc}. Two-dimensional abundance profiles representing the entire disk's chemical composition are presented in Sect. 3.6.

3.5.2.1 Oxygen chemistry

The main oxygen reservoir at the onset of collapse is H_2O ice (Sect. 3.4). Its abundance remains constant at 1×10^{-4} in our reference parcel until it gets to point C in Fig. 3.3, where it evaporates from the dust and is immediately photodissociated. When the parcel enters the disk, some H_2O is reformed to produce final gas-phase and solid abundances of $\sim 10^{-8}$ relative to n_H (Sect. 3.5.1.1).

Figure 3.4 shows the disk at t_{acc}, divided into seven zones according to different chemical evolutionary schemes for H_2O. The material in **zone 1** is the only material in the disk in which H_2O never evaporates during the collapse, because the temperature never gets high enough. The abundance is constant throughout zone 1 at t_{acc} at $\sim 1 \times 10^{-4}$ (see also

Table 3.3 – Abundances of selected species (relative to n_H) at $t = t_{acc}$ at four positions in the disk (two on the midplane, two at the surface).

Species	R = 6 AU, z = 0.0 AU	R = 24 AU, z = 0.0 AU	R = 6 AU, z = 2.0 AU	R = 24 AU, z = 6.0 AU
Zones[a]	7, 5, 8	7, 5, 8	2, 2, 5	1, 1, 2
H_2O	5(-7)	1(-12)	1(-8)	4(-9)
H_2O ice	1(-4)	1(-4)	7(-8)	8(-5)
O_2	1(-6)	6(-8)	1(-7)	1(-5)
O_2 ice	<1(-12)	<1(-12)	<1(-12)	<1(-12)
O	1(-6)	1(-6)	1(-4)	8(-7)
OH	2(-11)	<1(-12)	<1(-12)	9(-10)
CO	7(-5)	7(-5)	8(-5)	6(-5)
CO ice	<1(-12)	<1(-12)	<1(-12)	<1(-12)
CH_4	7(-8)	1(-7)	2(-9)	1(-5)
CH_4 ice	<1(-12)	<1(-12)	<1(-12)	<1(-12)
HCO^+	1(-12)	5(-11)	3(-12)	4(-12)
C	<1(-12)	<1(-12)	9(-12)	<1(-12)
C^+	<1(-12)	<1(-12)	<1(-12)	<1(-12)
N_2	1(-5)	1(-5)	1(-5)	5(-6)
N_2 ice	<1(-12)	<1(-12)	<1(-12)	<1(-12)
NH_3	5(-10)	2(-10)	4(-10)	8(-6)
NH_3 ice	<1(-12)	5(-9)	<1(-12)	5(-8)
NO	1(-8)	5(-10)	<1(-12)	6(-6)
NO ice	<1(-12)	<1(-12)	<1(-12)	<1(-12)
N_2H^+	<1(-12)	<1(-12)	<1(-12)	<1(-12)
N	5(-11)	1(-9)	5(-6)	4(-11)

[a] The H_2O, CH_4 and NH_3 zones from Figs. 3.4, 3.7 and 3.9 in which each position is located.

Table 3.3). For the material ending up in the other six zones, H_2O evaporates at some point during the collapse phase. **Zone 2** contains our reference parcel, so its H_2O history has already been described. The total H_2O abundance (gas and ice combined) at t_{acc} is $\sim 10^{-8}$ at the top of zone 2 and $\sim 10^{-6}$ at the bottom. The gas-ice ratio goes from ~1 at the top to $\sim 10^{-6}$ at the bottom.

The H_2O history of **zone 3** is the same as that of zone 2, except that it finishes with a gas-ice ratio larger than unity. In both cases H_2O evaporates and is photodissociated prior to entering the disk (point C in Fig. 3.3), and it partially reforms inside the disk (point D). Parcels ending up in **zone 4** also undergo the evaporation and photodissociation of H_2O. However, the low extinction in zone 4 against the stellar UV radiation prevents H_2O from reforming like it does in zones 2 and 3.

The material in **zone 5** has a rather different history from that in zones 2–4 because it enters the disk at an earlier time: between $t = 1.3 \times 10^5$ and 2.3×10^5 yr. The material in

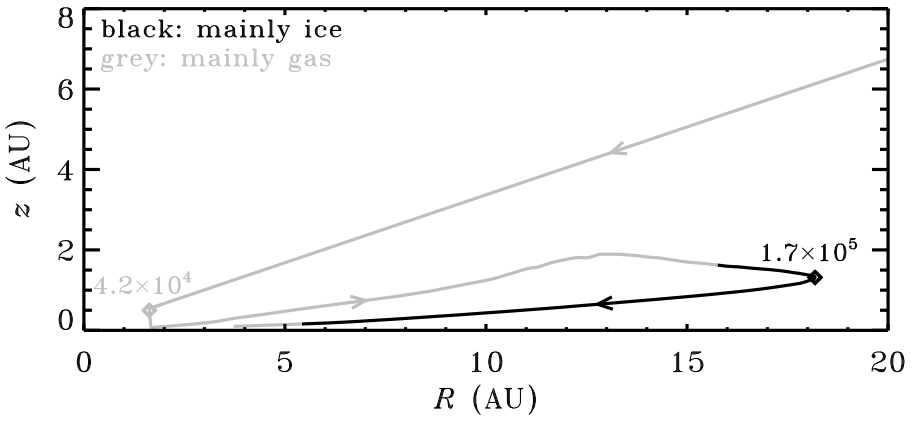

Figure 3.5 – Infall trajectory for a parcel ending up in zone 6 from Fig. 3.4, showing where H_2O is predominantly present as ice (black) or gas (grey). The two diamonds mark the time in years after the onset of collapse.

zones 2–4 all accretes after $t = 2.4 \times 10^5$ yr. The infall trajectories terminating in zone 5 do not pass close enough to the outflow wall or the inner disk surface for photoprocesses to play a role. All H_2O in zone 5 is in the gas phase at $t_{\rm acc}$ (abundance: 1×10^{-4}) because it lies inside the disk's snow line. The evaporation of H_2O ice does not occur until the material actually crossed the snow line. Prior to that point, the temperature never gets high enough for H_2O to leave the grains.

Moving to **zones 6 and 7**, we find material that accretes even earlier: at $t = 4 \times 10^4$ yr. The disk at that time is only 2 AU large and several 100 K hot, so the ice mantles are completely removed. Instead of carrying on towards the star, this material remains part of the disk and is transported outwards to conserve angular momentum. Figure 3.5 shows the path followed by one particular parcel terminating in zone 6. As indicated by the initial grey portion of the line, H_2O has already evaporated (at $R = 25$ AU, not shown) before entering the young disk. The parcel cools down during the outward part of the trajectory and H_2O returns to the solid phase. At $t = 1.7 \times 10^5$ yr, the parcel starts moving inwards again and comes close enough to the protostar for H_2O to evaporate a second time. Other parcels ending up in zone 6 have similar trajectories and the same qualitative H_2O history. The parcels ending up in zone 7 also have H_2O evaporating during the initial infall and freezing out again during the outward part of the trajectory. However, they do not terminate close enough to the protostar for H_2O to desorb a second time. Therefore, most H_2O in zone 7 at $t_{\rm acc}$ is on the grains.

Our model is not the first one in which part of the disk contains H_2O that evaporated and readsorbed. Lunine et al. (1991), Owen et al. (1992) and Owen & Bar-Nun (1993) argued that the accretion shock at the surface of the disk is strong enough for H_2O to evaporate. However, based on the model of Neufeld & Hollenbach (1994), we showed in

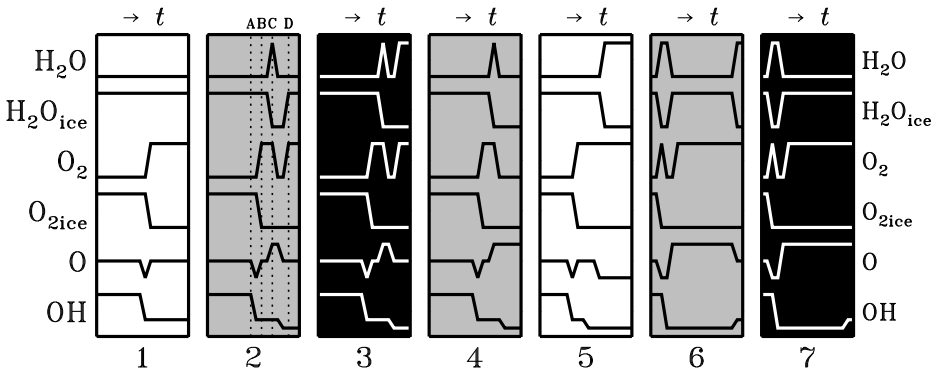

Figure 3.6 – Qualitative evolution of some abundances towards the seven zones with different H_2O histories from Fig. 3.4. The horizontal axes show the time (increasing from left to right) and are non-linear. The position of points A, B, C and D from Fig. 3.3 is indicated for zone 2, which contains our reference parcel.

Chapter 2 that most of the disk material does not pass through a shock that heats the dust to 100 K or more. Moreover, the material that does get shock-heated to that temperature accretes close enough to the star that the stellar radiation already heats it to more than 100 K. Hence, including the accretion shock explicitly in our model would at most result in minor changes to the chemistry.

As discussed in Sect. 3.5.1.1, H_2O controls part of the oxygen chemistry along the infall trajectory of our reference parcel, and it does the same thing for other parcels. Figure 3.6 presents a schematic view of the chemical evolution of six oxygen-bearing species towards each of the seven zones from Fig. 3.4. The abundances are indicated qualitatively as high, intermediate or low. The horizontal axes (time, increasing from left to right) are non-linear and only indicate the order in which various events take place.

For material ending up in **zone 1**, H_2O never evaporates, but O_2 does. OH is inititally relatively abundant but most of it disappears when the overall density increases and the reactions with O, N and H_3^+ become faster. The abundance of atomic O experiences a drop at the same time, but it goes back up shortly after due to the evaporation of CO, O_2 and NO followed by Reactions (3.30)–(3.32). O_2 also evaporates on its way to **zones 2, 3 and 4** and because it passes through an area of low extinction, it is subsequently photodissociated. This, together with the photodissociation of OH and H_2O, causes an increase in the abundance of atomic O. Zones 2 and 3 are sufficiently shielded against the stellar UV field, so O_2 is reformed at the end of the trajectory. This does not happen in the less extincted zone 4.

Material ending up in **zone 5** has the same qualitative history for gas-phase and solid O_2 as has material ending up in zone 1. The evolution of atomic O initially also shows the same pattern, but it experiences a second drop as the total density becomes even higher than it does for zone 1. The higher density also causes an additional drop in the

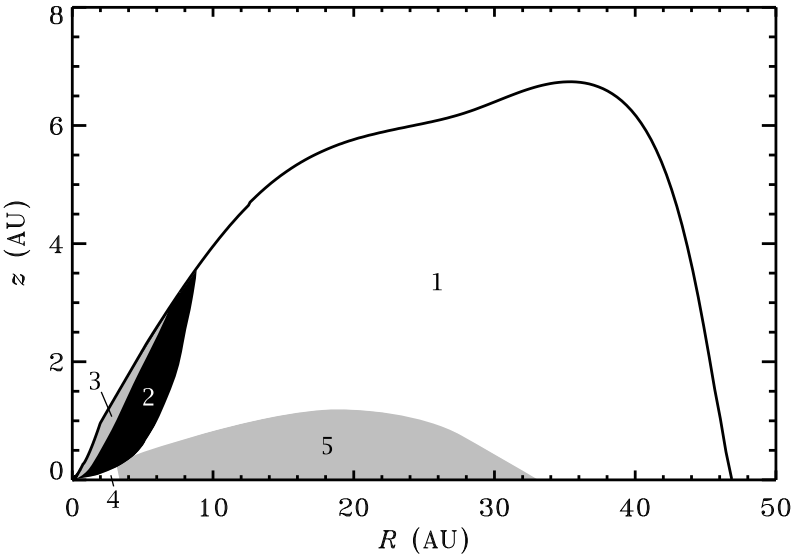

Figure 3.7 – As Fig. 3.4, but for CH_4 gas and ice. The main carbon reservoir at t_{acc} is CO gas throughout the disk.

OH abundance. En route towards **zones 6 and 7**, O_2 evaporates and is photodissociated during the early accretion onto the small disk. It is reformed during the outward part of the trajectory and survives until t_{acc}. Atomic O is also relatively abundant along most of the trajectory, although always one or two orders of magnitude below O_2. In zone 6, the O abundance decreases at the end due to the reaction with evaporating CH_3, producing H_2CO and H. Zone 7 does not get warm enough for CH_3 to evaporate, so O remains intact.

3.5.2.2 Carbon chemistry

The two main carbon reservoirs at the onset of collapse are CO ice and CH_4 ice (Sect. 3.4). Their binding energies are relatively low (855 and 1080 K), so they evaporate throughout the core soon after the collapse begins (Sect. 3.5.1.2). For our reference parcel, the main difference between the evolution of CO and CH_4 is the photodissociation of the latter (near point C in Fig. 3.3) while the former remains intact. Following our approach for H_2O, we can divide the disk at t_{acc} into several zones according to different chemical evolution scenarios for CO. However, the entire disk has the same qualitative CO history: apart from evaporating early on in the collapse phase, CO does not undergo any processing (cf. Chapter 2). Hence, we divide the disk according to the evolution of CH_4 instead (Fig. 3.7).

For material that ends up in **zone 1**, the only chemical process for CH_4 is the evaporation during the initial warm-up of the core. It is not photodissociated at any point

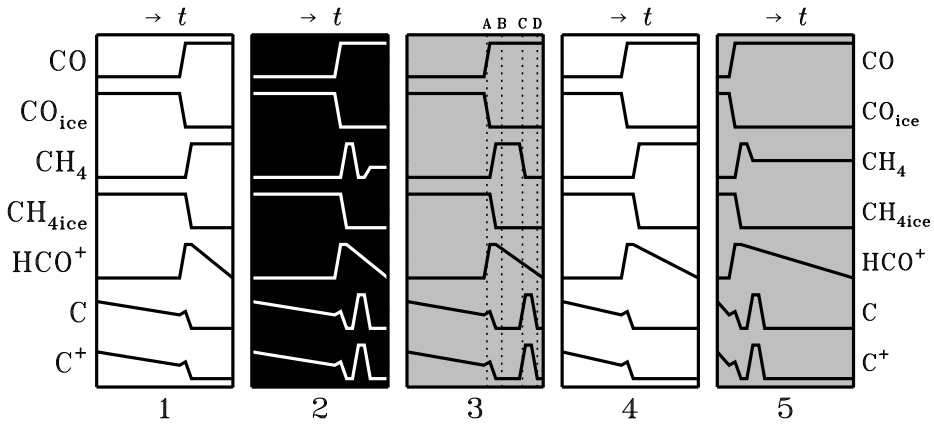

Figure 3.8 – As Fig. 3.6, but for the five zones with different CH_4 histories from Fig. 3.7.

during the collapse, nor does it freeze out again or react significantly with other species. Material ending up closer to the star, in **zones 2 and 3**, is sufficiently irradiated by the stellar UV/visible field for CH_4 to be photodissociated. Zone 3, which contains our reference parcel, is hardly shielded from the stellar flux and the final CH_4 abundance is only a few 10^{-10}. The stronger extinction towards zone 2 allows CH_4 to be reformed at a final abundance of 10^{-9}–10^{-7} relative to n_H (Table 3.3).

Zone 4 contains material that accretes onto the disk several 10^4 yr earlier than does the material in zones 2 and 3. It always remains well shielded from the stellar radiation, so the only processing of CH_4 is the evaporation during the early parts of the collapse. The CH_4 history of zones 1 and 4 is thus qualitatively the same. The last zone, **zone 5**, consists of material that accretes around $t = 4\times10^4$ yr and is subsequently transported outwards to conserve angular momentum (Fig. 3.5). CH_4 in this material evaporates before entering the young disk and is photodissociated as it gets within a few AU of the protostar. The resulting atomic C is mostly converted into CO and remains in that form for the rest of the trajectory. Hence, even though the extinction decreases again when the parcel moves outwards, no CH_4 is reformed.

The evolution of the abundances of CH_4 gas and ice, CO gas and ice, HCO^+, C and C^+ towards each of the five zones is plotted schematically in Fig. 3.8. As noted in Sect. 3.5.1.2, the HCO^+ abundance follows the CO abundance at a ratio that is roughly inversely proportional to the overall density. Hence, the HCO^+ evolution is qualitatively the same towards each zone: it reaches a maximum abundance of a few 10^{-10} when CO evaporates and gradually disappears as the density increases along the rest of the infall trajectories. The most complex history amongst these seven carbon-bearing species is found in C and C^+. Towards all five zones, they are initially destroyed by reactions with H_2, O_2 and OH. Some C and C^+ is reformed when CO evaporates (at point A in Fig. 3.3), but the subsequent evaporation of O_2 and OH causes the abundances to decrease again. En route

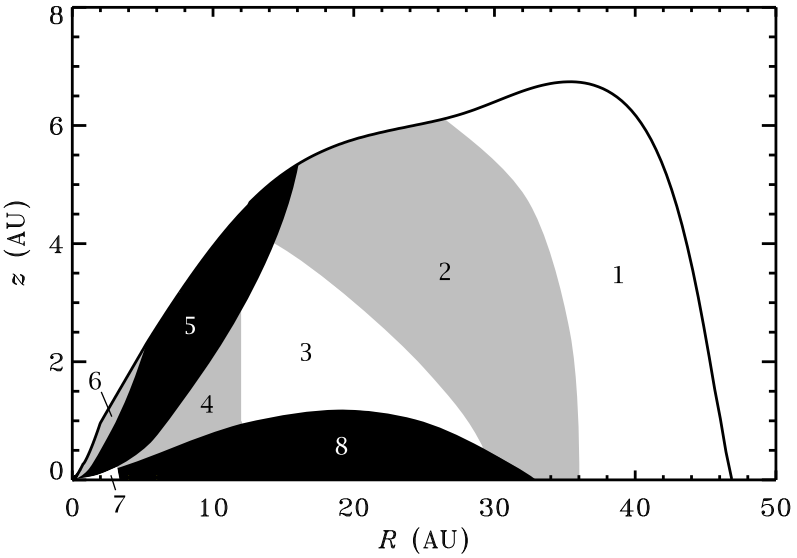

Figure 3.9 – As Fig. 3.4, but for NH_3 gas and ice. The main nitrogen reservoir at t_{acc} is N_2 gas throughout the disk.

to zones 2, 3 and 5, the photodissociation of CH_4 leads to a second increase in C and C^+, followed by a third and final decrease when the parcel moves into a more shielded area.

3.5.2.3 Nitrogen chemistry

Most nitrogen at the onset of collapse is in the form of solid N_2 (41%), solid NH_3 (32%) and solid NO (22%). The evolution of N_2 during the collapse is the same as that of CO, except for a minor difference in the binding energy. Both species evaporate shortly after the collapse begins and remains in the gas phase throughout the rest of the simulation. Neither one is photodissociated because they need UV photons shortwards of 1100 Å, and the protostar is not hot enough to provide those.

The evolution of NH_3 shows a lot more variation, as illustrated in Fig. 3.9. The disk at t_{acc} is divided into eight zones with different NH_3 histories. No processing occurs towards **zone 1**: the temperature never exceeds the 73 K required for NH_3 to evaporate, so it simply remains on the grains the whole time. Material ending up in **zone 2** does get heated above 73 K, so NH_3 evaporates. However, it freezes out again at the end of the trajectory because zone 2 itself is not warm enough to sustain gaseous NH_3. The final solid NH_3 abundance in zones 1 and 2 is about 8×10^{-6} relative to n_H (Table 3.3).

NH_3 ending up in **zone 3** also evaporates from the grains just before entering the disk. It is then destroyed by UV photons (only for material that ends up inside of 15 AU in zone 3) and by HCO^+ (for all material in zone 3). Towards the end of the trajectory, some NH_3 is reformed from the dissociative recombination of NH_4^+ and this immediately freezes out

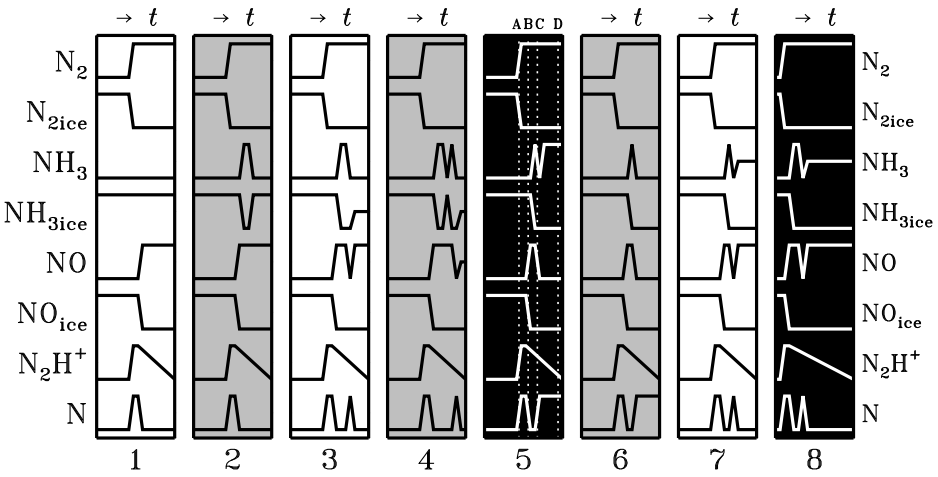

Figure 3.10 – As Fig. 3.6, but for the eight zones with different NH_3 histories from Fig. 3.9.

to produce a final solid NH_3 abundance of 10^{-10}–10^{-8}. **Zone 4** has the same history, except that there is an additional adsorption-desorption cycle before the destruction by photons and HCO^+.

Our standard parcel ends up in **zone 5**; its NH_3 evolution is mainly characterised by photodissociation above the disk and reformation inside it (Sect. 3.5.1.3). As is the case for zones 2–4, NH_3 evaporates when it gets to within about 200 AU of the star, halfway between points B and C in Fig. 3.3. It is immediately photodissociated, but some NH_3 is reformed once the material is shielded from the stellar radiation. The reformed NH_3 remains in the gas phase. No reformation takes place in the less extincted **zone 6**, which otherwise has the same NH_3 history as does zone 5.

Material ending up in **zone 7** does not pass close enough to the outflow wall for NH_3 to be photodissociated upon evaporation. Instead, NH_3 is mainly destroyed by HCO^+ and attains a final abundance of $\sim 10^{-9}$. Lastly, **zone 8** contains again the material that accretes onto the disk at an early time and then moves outwards to conserve angular momentum. Its NH_3 evaporates already before reaching the disk and is subequently dissociated by the stellar UV field. As the material moves away from the star and is shielded from its radiation, some NH_3 is reformed out of NH_4^+ to a final abundance of $\sim 10^{-10}$.

The abundances of N_2H^+ and atomic N are largely controlled by the evolution of N_2 and NH_3, as shown schematically in Fig. 3.10. In all parcels, regardless of where they end up, N_2H^+ is mainly formed out of N_2 and H_3^+, so its abundance goes up when N_2 evaporates shortly after the onset of collapse. It gradually disappears again as the collapse proceeds due to the inverse relationship between the overall density and the N_2H^+-N_2 ratio (Eq. (3.47)). The atomic N abundance at the onset of collapse is 1×10^{-7}. It increases when N_2 evaporates and decreases again a short while later when NO evaporates (Sect. 3.5.1.3). For material that ends up in zones 1 and 2, the N abundance is mostly constant

for the rest of the collapse at a value of 10^{-13} (inner part of zone 2) to 10^{-10} (outer part of zone 1). Material that ends up in the other six zones is exposed to enough UV radiation for NO and NH_3 to be photodissociated, so there is a second increase in atomic N. Zones 3, 4, 7 and 8 are sufficiently shielded at t_{acc} to reform some or all NO and NH_3, and the N abundance finishes low. Less reformation is possible in zones 5 and 6, so they have a relatively large amount of atomic N at the end of the collapse phase.

3.5.2.4 Mixing

Given the dynamical nature of circumstellar disks, the zonal distribution presented in the preceding subsections may offer too simple a picture of the chemical composition. For one thing, there are as yet no first principles calculations of the processes responsible for the viscous transport in disks. The radial velocity equation used in our model (see Chapter 4) is suitable as a zeroth-order description, but cannot explain important observational features like episodic accretion (Kenyon & Hartmann 1995, Evans et al. 2009). The radial velocity profile in real disks is probably much more chaotic, so there would be more mixing between adjacent zones. Hence, both the shapes and the locations of the zones are likely to be different from what is shown in Figs. 3.4, 3.7 and 3.9. A larger degree of mixing would also make the borders between the zones more diffuse than they are in our simple schematic representation. Nevertheless, the general picture from this section offers a plausible description of the chemical history towards different parts of the disk. Spectroscopic observations at AU resolution, for example with the upcoming Atacama Large Millimeter/submillimeter Array (ALMA), are required to determine to what extent this picture holds in reality.

3.6 Chemical history versus local chemistry

Section 3.5 contains many examples of abundances increasing or decreasing on short timescales of less than a hundred years (see, e.g., Fig. 3.2). It appears that the abundances respond rapidly to the changing physical conditions as material falls in supersonically through the inner envelope and accretes onto the disk. However, this does not necessarily mean that the abundances are always in equilibrium. In this section we explore the question as to whether the disk is in chemical equilibrium at the end of the collapse, or if its chemical composition is a non-equilibrium solution to the conditions encountered during the collapse phase. To that end, we evolve the chemistry for an additional 1 Myr beyond t_{acc}. We keep the density, temperature, UV flux and extinction constant at the values they have at t_{acc}, and we also keep all parcels of material at the same position. Clearly, this is a purely hypothetical scenario. In reality, the disk would change in many ways after t_{acc}: it spreads in size (see Chapter 4), the surface layers become more strongly irradiated, the temperature changes, the dust coagulates into planetesimals, gas is photoevaporated from the surface layers, and so on. All of these processes have the potential to affect the chemical composition. However, they would also interfere with our attempt to determine whether the disk is in chemical equilibrium at t_{acc}. This question is most easily addressed

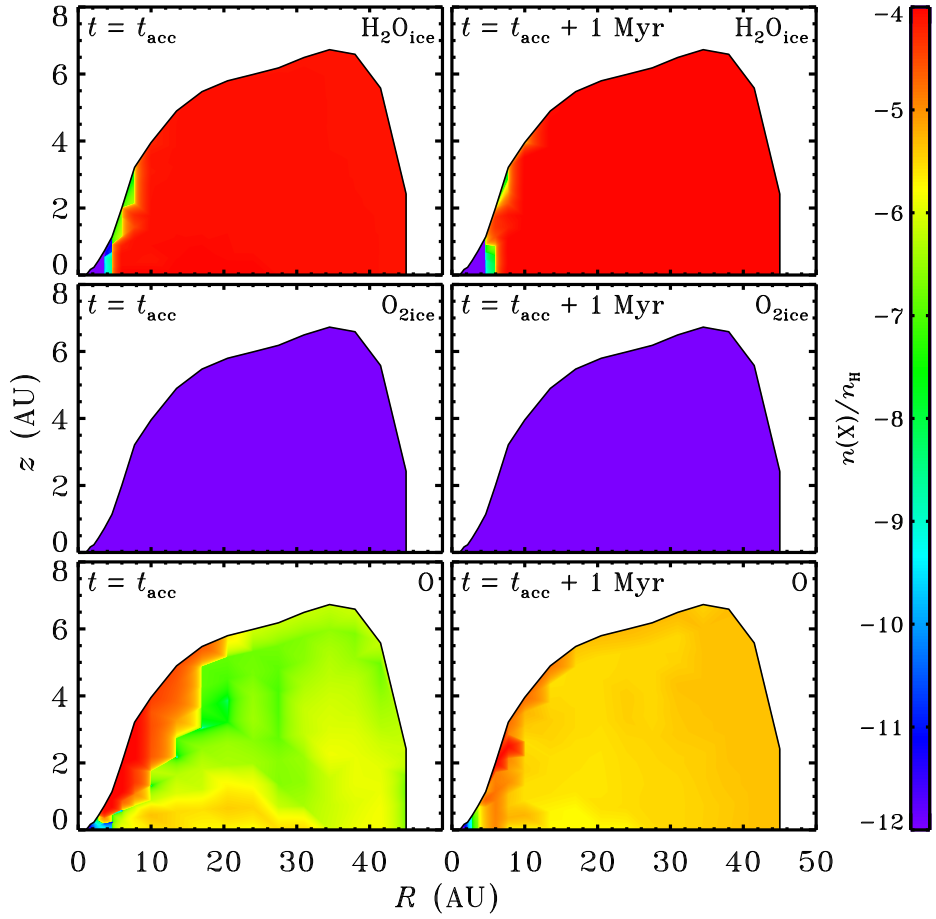

Figure 3.11 – Abundances of H_2O ice, O_2 ice and gaseous atomic O throughout the disk at the end of the collapse phase ($t = t_{acc}$) and after an additional static post-collapse phase of 1 Myr.

by evolving the chemistry for an additional period of time at constant conditions, hence we ignore all of the physical changes that would normally occur during the post-collapse phase.

The abundance profiles for the oxygen-, carbon- and nitrogen-bearing species from the previous sections are plotted in Figs. 3.11–3.17. In each case, the left panel corresponds to the end of the collapse phase ($t = t_{acc}$) and the right panel to the end of the static 1 Myr post-collapse phase ($t = t_{acc}$ + 1 Myr). Abundances of less than 10^{-12} are unreliable in our chemical code, so lower values are not plotted. Hence, the purple areas in the figures should be interpreted as upper limits.

The 21 species in Figs. 3.11–3.17 can be divided into two categories: those whose

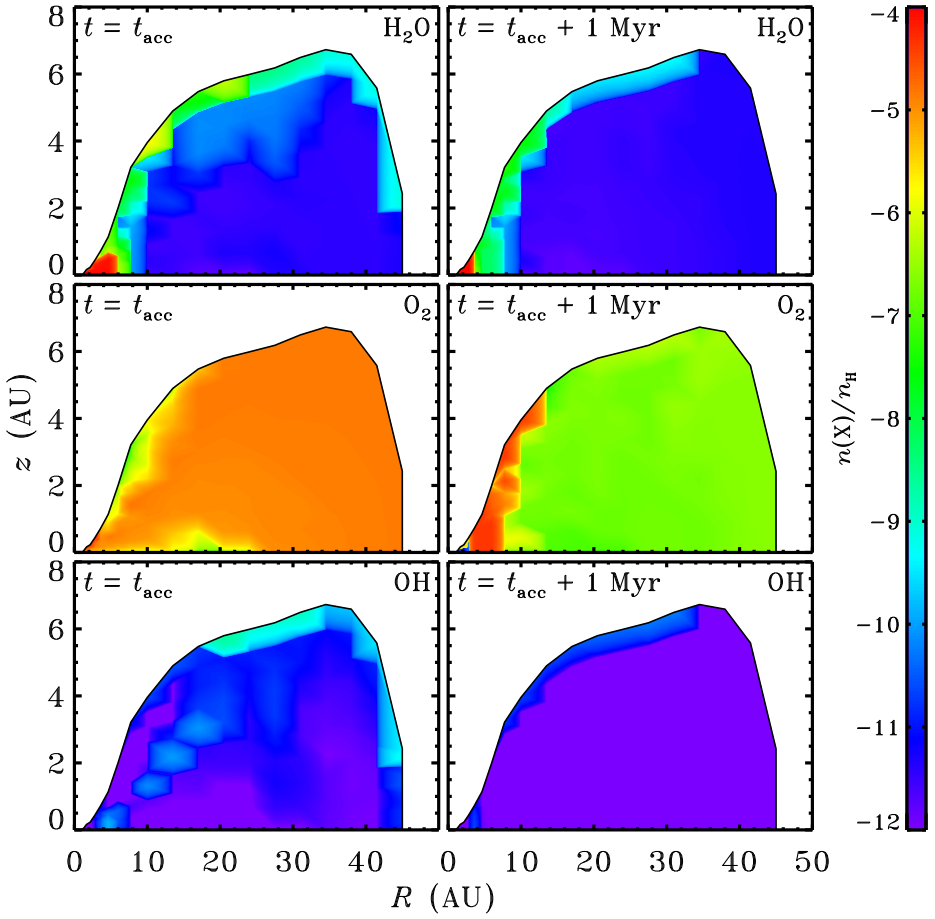

Figure 3.12 – As Fig. 3.11, for gaseous H_2O, O_2 and OH.

abundance profile changes during the post-collapse phase, and those whose abundance profile remains practically the same. Members of the former category are O_2, OH, CH_4, NH_3 and NO (all gaseous), NH_3 ice, and atomic O and N. The thirteen species in the "unchanged" category are H_2O gas and ice, O_2 ice, CO gas and ice, CH_4 ice, C, C^+, N_2 gas and ice, NO ice, HCO^+ and N_2H^+. The individual gas and ice abundances are summed in Fig. 3.18. The total H_2O, CO and N_2 abundances do not change significantly during the post-collapse phase, while the total O_2, CH_4, NH_3 and NO abundances change by more than two orders of magnitude in a fairly large part of the disk.

There are two areas in the disk where the abundances generally change the least: near the surface out to $R \approx 10$ AU, and at the midplane between ~5 and ~25 AU. In the first area, the chemistry is dominated by fast photoprocesses, allowing the abundances to reach

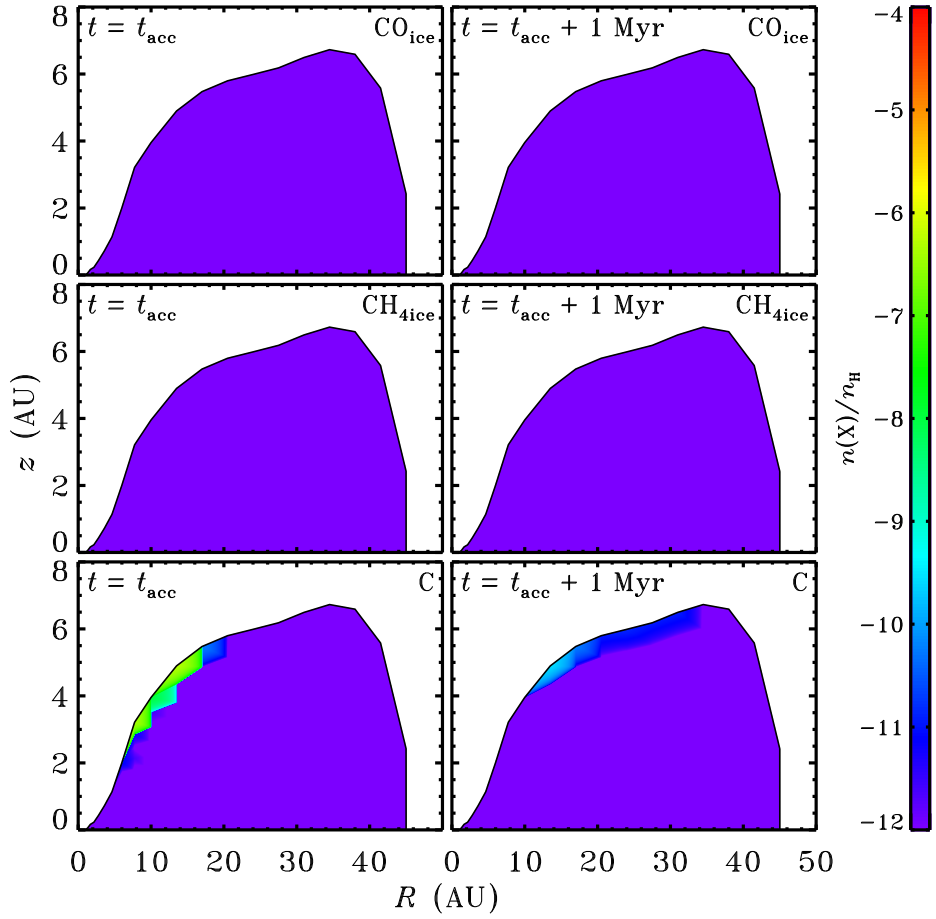

Figure 3.13 – As Fig. 3.11, for CO ice, CH_4 ice and gaseous atomic C.

equilibrium on short timescales. The second area, near the midplane, is the densest part of the disk and therefore has high collision frequencies and short chemical timescales. In addition, this part of the disk is populated by material that accreted at an early time (Fig. 3.5). The physical conditions it encountered during the rest of the collapse phase were relatively constant, aiding in establishing chemical equilibrium.

Outside these two "equilibrium areas", one of the key processes during the post-collapse phase is the conversion of gas-phase oxygen-bearing species into H_2O, which subsequently freezes out. Because H_2O ice already is one the main oxygen reservoirs at t_{acc} throughout most of the disk, its abundance only increases by about 20% during the rest of the simulation (Fig. 3.11). These 20% represent 10% of the total oxygen budget and correspond to 2×10^{-5} oxygen nuclei per hydrogen nucleus. One of the species converted

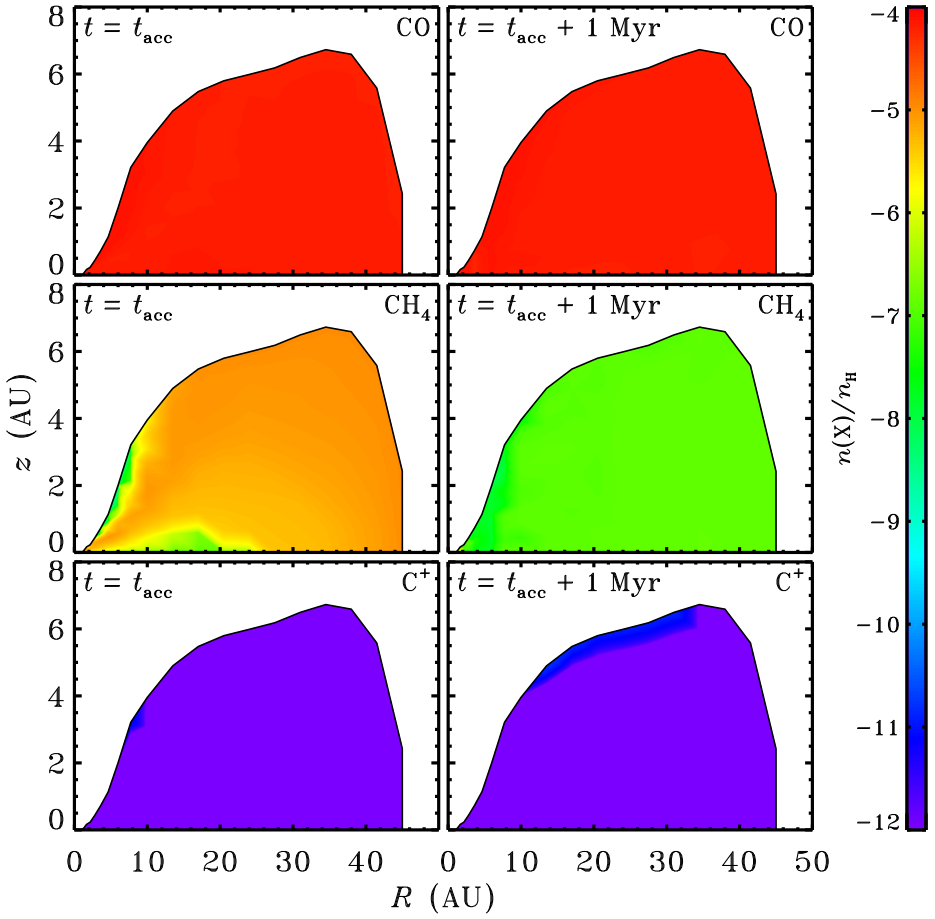

Figure 3.14 – As Fig. 3.11, for gaseous CO, CH_4 and C^+.

into H_2O ice is NO, which reacts with NH_2 through

$$NH_2 + NO \rightarrow N_2 + H_2O, \tag{3.58}$$

followed by adsorption of H_2O onto the dust. This reaction is responsible for the post-collapse destruction of gas-phase NO outside the two "equilibrium areas", as well as for the small increase (~20%) in gas-phase N_2 (Fig. 3.16). NO is the main destructor of atomic N via

$$NO + N \rightarrow N_2 + O, \tag{3.59}$$

so the conversion of NO into H_2O also explains the increased N abundance from Fig.

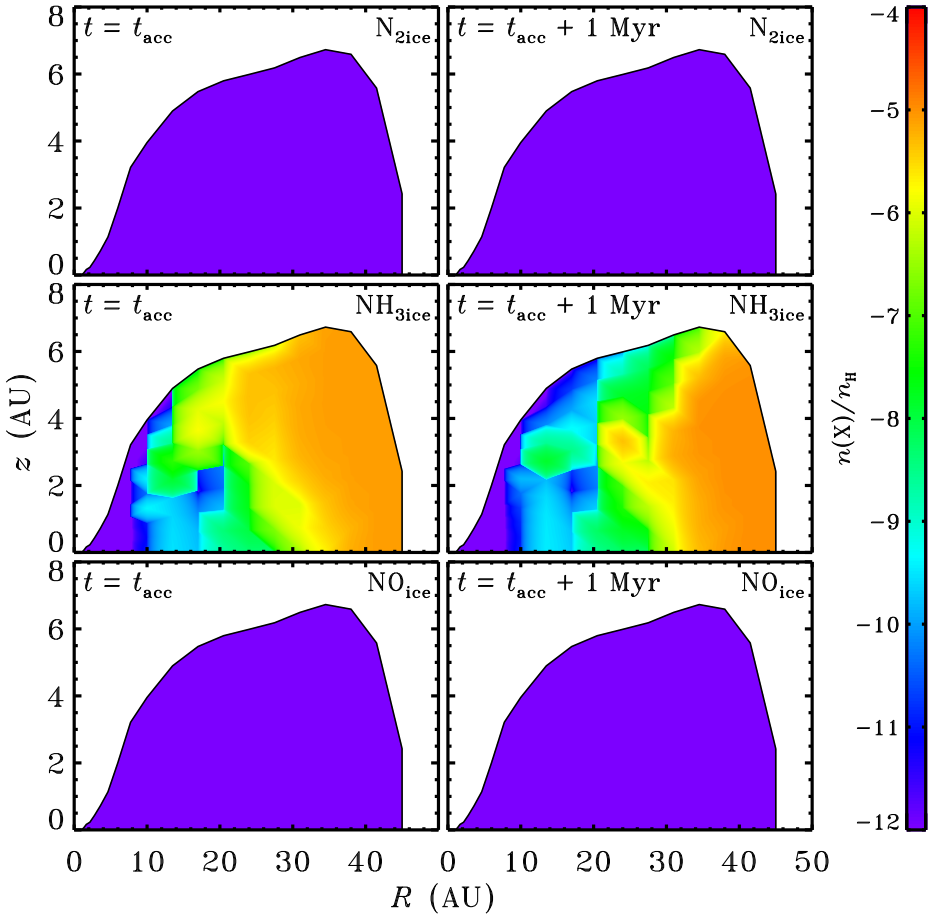

Figure 3.15 – As Fig. 3.11, for N_2 ice, NH_3 ice and NO ice.

3.17. The NH_2 required for Reaction (3.58) is formed from NH_3:

$$NH_3 + HCO^+ \rightarrow NH_4^+ + CO\,, \tag{3.60}$$

$$NH_4^+ + e^- \rightarrow NH_2 + H_2/2H\,. \tag{3.61}$$

The gas-phase reservoir of NH_3 is continously fed by evaporation of NH_3 ice, so Reactions 3.60, 3.61 and 3.58 effectively transform all NH_3 into N_2 (Figs. 3.15 and 3.16).

Two other species that are destroyed in the post-collapse phase are gaseous O_2 and CH_4 (Figs. 3.12 and 3.14). O_2 is ionised by cosmic rays to produce O_2^+, which then reacts with CH_4:

$$CH_4 + O_2^+ \rightarrow HCOOH_2^+ + H\,, \tag{3.62}$$

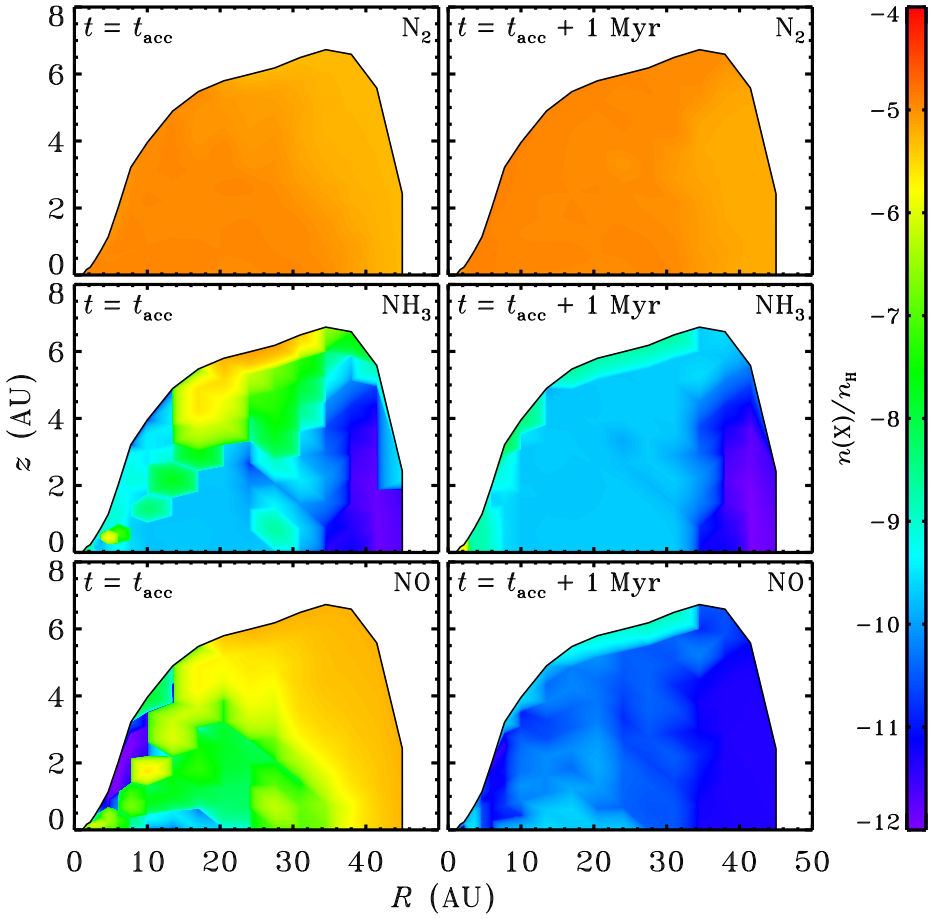

Figure 3.16 – As Fig. 3.11, for gaseous N_2, NH_3 and NO.

$$HCOOH_2^+ + e^- \rightarrow HCOOH + H\,. \tag{3.63}$$

The formic acid (HCOOH) freezes out, thus acting as a sink for both carbon and oxygen. At $t = t_{acc} + 1$ Myr, the solid HCOOH abundance is 3×10^{-6}, accounting for 3% of all oxygen and 4% of all carbon. The presence of such a sink is a common feature of disk chemistry models. Gas-phase species are processed by He^+ and H_3^+ until they form a species whose evaporation temperature is higher than the dust temperature. This is HCOOH in our case, but it could also be carbon-chain molecules like C_2H_2 or C_3H_4 (Aikawa & Herbst 1999). Another important post-collapse sink reaction in our model is the freeze-out of HNO. At t_{acc}, OH is primarily formed by

$$HNO + O \rightarrow NO + OH \tag{3.64}$$

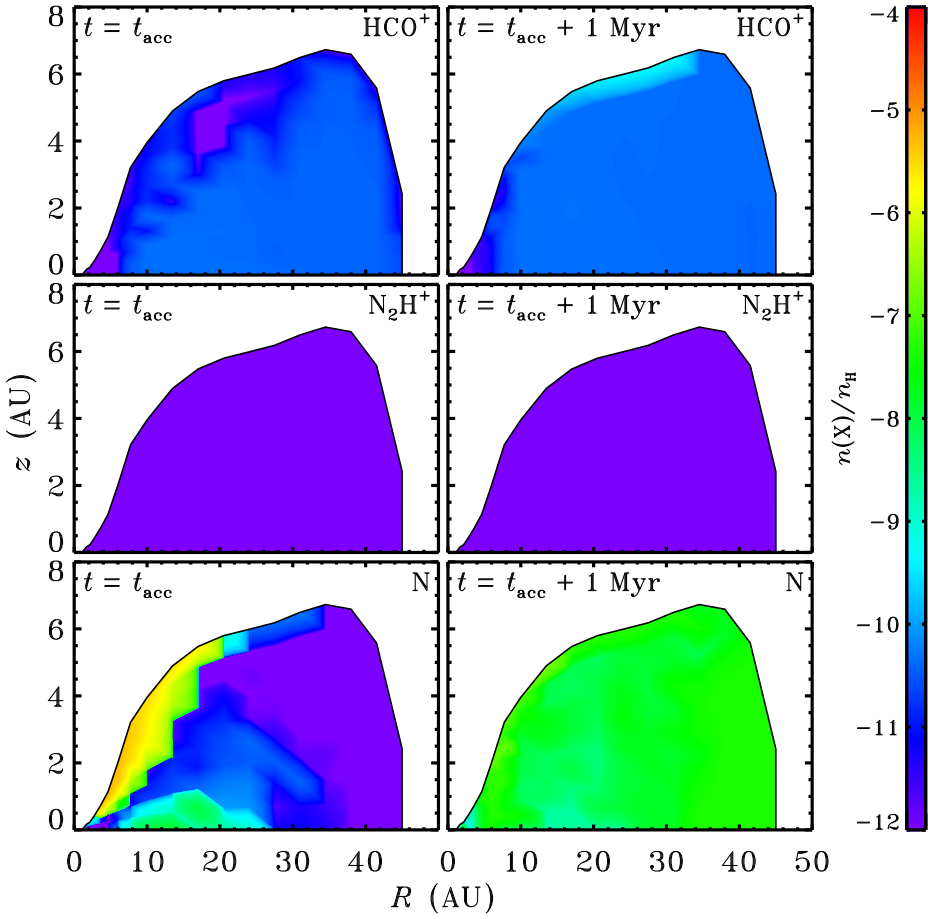

Figure 3.17 – As Fig. 3.11, for HCO^+, N_2H^+ and atomic N.

throughout most of the disk. This reaction is also one of the main destruction channels for atomic O. Hence, the gradual freeze-out of HNO after t_{acc} leads to a decrease in OH and an increase in O (Figs. 3.11 and 3.12). Also contributing to the higher O abundance is the fact that OH itself is an important destructor of O through Reaction (3.13).

The post-collapse chemistry described here is merely meant as an illustration of what might take place in a real circumstellar disk after the main accretion phase comes to an end. Depending on how the disk continues to evolve physically, other reactions may become more important than the ones listed above. However, it is clear that, in general, the disk is not in chemical equilibrium at t_{acc}. Figures 3.11–3.18 show several examples of abundances changing by a few orders of magnitude. Even the two "equilibrium areas" (near the surface out to 10 AU and from 5 to 25 AU at the midplane) are not truly in

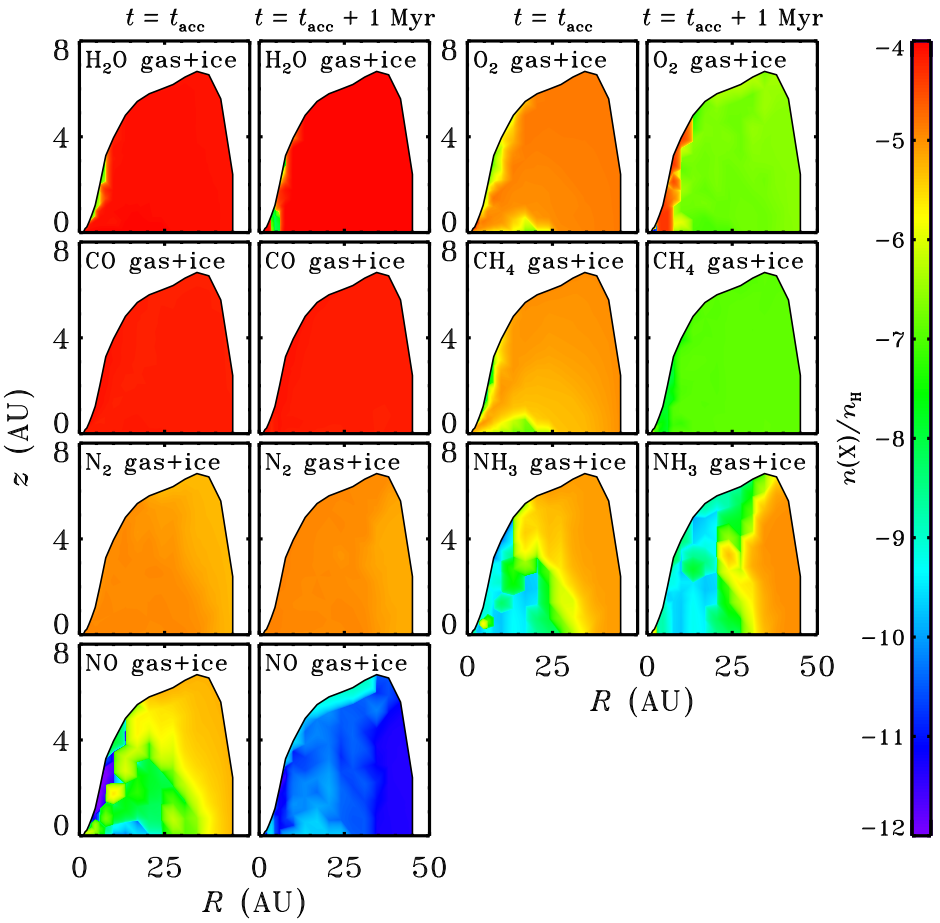

Figure 3.18 – Abundances of total H_2O, O_2, CO, CH_4, N_2, NH_3 and NO (gas and ice combined) throughout the disk at the end of the collapse phase ($t = t_{acc}$) and after an additional 1 Myr post-collapse phase ($t = t_{acc}$ + 1 Myr).

chemical equilibrium. For example, at 20 AU on the midplane, the abundances of solid HCOOH, C_2O, C_3O and CH_3OH increase by factors of 10 to 25 during the post-collapse processing.

As the disk evolves from the end of the collapse phase to a mature T Tauri disk, it spreads to larger radii. At the same time, material continues to accrete onto the protostar and gas is evaporated from the surface layers by the stellar radiation field. Altogether, this results in lower gas densities and longer chemical timescales. It is therefore unlikely that the gas will ever reach chemical equilibrium, as is indeed confirmed by chemical models

of T Tauri disks (Fegley 2000). Hence, some signature of the collapse-phase chemistry may survive into later stages. This will be the topic of a future publication.

3.7 Discussion

3.7.1 Caveats

Several caveats were mentioned in the preceding sections, which we briefly discuss here. First of all, our model does not calculate the gas temperature explicitly, but simply sets it equal to the dust temperature. This approach is valid for the interior of the disk (optically thick to UV radiation), but it breaks down in the surface layers and in the inner parts of the envelope (Kamp & Dullemond 2004, Jonkheid et al. 2004, Woitke et al. 2009). The chemistry in these optically thin regions is mostly controlled by photoprocesses and ion-molecule reactions, neither of which depend strongly on temperature. One aspect that would be affected is the gas-phase production of H_2O through the reactions

$$O + H_2 \rightarrow OH + H, \tag{3.65}$$

$$OH + H_2 \rightarrow H_2O + H, \tag{3.66}$$

which have activation barriers of 3100 and 1700 K, respectively (Natarajan & Roth 1987, Oldenborg et al. 1992). Hence, our model probably underestimates the amount of H_2O in the surface of the disk. Other than that, increasing the gas temperature to a more realistic value is unlikely to change the chemical results. Taking a higher gas temperature might change some of the physical structure. It would increase the pressure of the disk, thus pushing up the disk-envelope boundary and possibly changing the spatial distribution of where material accretes onto the disk. However, the bulk of the accretion currently takes place in optically thick regions, so only a small fraction of the infalling material would be affected.

The shape of the stellar spectrum may have larger chemical consequences. Right now, we simply take a blackbody spectrum at the effective stellar temperature. Our star never gets hotter than 5800 K, which is not enough to produce UV photons of sufficient energy to dissociate CO and H_2. Many T Tauri stars are known to have a UV excess, which *would* allow CO and H_2 to be photodissociated. The stronger UV flux would also enhance the photoionisation of atomic C, probably resulting in C^+ being the dominant form of carbon between points C and D in Fig. 3.3. In turn, this would boost the production of carbon-chain species like C_2S and HC_3N. As soon as the material enters the disk and is shielded again from the stellar radiation, C^+ is converted back into C and CO. However, some signature of the temporary high C^+ abundance may survive.

The third caveat has to do with the trapping of volatile species like CO, CH_4 and N_2 in the H_2O ice matrix. We argued in Chapter 2 that trapping of CO is required to explain the observed abundances of CO in comets. In the full chemical network from the current chapter, trapping of CO and other volatiles would reduce their gas-phase abundances, which in turn may reduce their controlling role in the gas-phase chemistry. However, the

trapped fraction is never more than 30% (Viti et al. 2004, Fayolle et al. in prep.; see also Gibb et al. 2004), so their gas-phase abundances remain high compared to other species. Hence, CO, CH_4, N_2, O_2 and NO are still likely to control the gas-phase chemistry even if they are partially trapped on the dust grains.

3.7.2 Comets

The chemical composition of cometary ices shows many similarities to that of sources in the ISM, but the abundance of a given species may vary by more than an order of magnitude from one comet to the next (A'Hearn et al. 1995, Bockelée-Morvan et al. 2000, 2004, Schöier et al. 2002, Ehrenfreund et al. 2004, Disanti & Mumma 2008). Both points are illustrated in Fig. 3.19, where the abundances of several species in the comets 1P/Halley, C/1995 O1 (Hale-Bopp), C/1996 B2 (Hyakutake), C/1999 H1 (Lee), C/1999 S4 (LINEAR) and 153P/Ikeya-Zhang are plotted against the abundances in the embedded protostar IRAS 16293–2422 (warm inner envelope), the bipolar outflow L1157, and the four hot cores W3(H_2O), G34.3+0.15, Orion HC and Orion CR. Each point is characterised by the mean value from the available sources (the diamonds) and the total spread in measurements (the error bars). Uncertainties from individual measurements are not shown. The dotted line marks the theoretical relationship where the ISM abundances equal the cometary abundances. The data generally follow this line, suggesting that the material ending up in comets underwent little chemical processing from the ISM. However, the plot also shows variations of at least an order of magnitude in the cometary abundances for CO, H_2CO, CH_3OH, HNC, H_2S and S_2, as well as smaller variations for other species. These different chemical compositions may be explained by assuming that the comets were formed in different parts of the solar nebula. If that is indeed the case, there must have been some degree of chemical processing between the ISM and the cometary nuclei. Another point to note is that the elemental nitrogen abundance in comets is at least a factor of three lower than that in the ISM (Wyckoff et al. 1991, Jessberger & Kissel 1991, Bockelée-Morvan et al. 2000). Although the reason for this deficiency remains unclear, it does also point at a certain degree of chemical processing.

Comets are thought to have formed at the gravitational midplane of the circumsolar disk, between 5 and 30 AU from the young Sun (Bockelée-Morvan et al. 2004, Kobayashi et al. 2007). In our model disk, the 5–30 AU range happens to be almost exactly the area containing material that accreted at an early time (4×10^4 yr after the onset of collapse) and stayed in the disk for the remainder of the collapse phase (Fig. 3.5). As discussed in Sect. 3.5.2, this material undergoes a larger degree of chemical processing than any other material in the disk, due to its accreting close to the star. If comets are entirely formed out of such material, it is hard to reconcile the large degree of processing with the observed similarities between cometary and ISM abundances. It requires that either the abundances of observed cometary species actually remain constant throughout the collapse, or that they return to ISM values after the material reaches its final position. In this section we argue that neither scenario is likely to be true, and that the similarity between cometary and ISM abundances in fact results from mixing unprocessed material from other parts of the disk into the comet-forming zone.

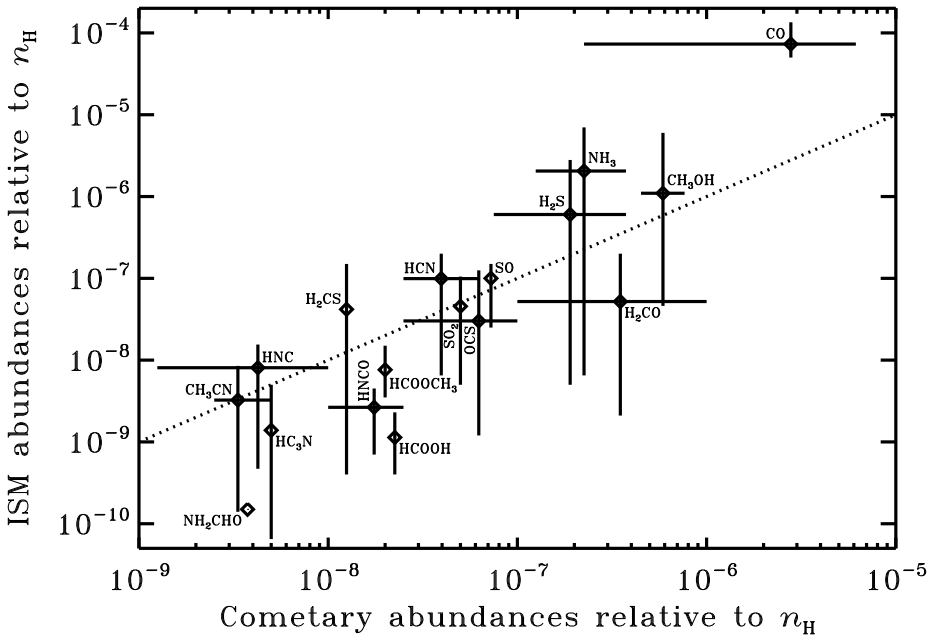

Figure 3.19 – Molecular abundances in comets (Halley, Hale-Bopp, Hyakutake, Lee, C/1999 S4 and Ikeya-Zhang) compared to those in ISM sources (IRAS 16293–2422 (warm inner envelope), L1157, W3(H_2O), G34.3+0.15, Orion Hot Core and Orion Compact Ridge) as provided by Bockelée-Morvan et al. (2000, 2004) and Schöier et al. (2002). The error bars indicate the spread between sources; errors from individual measurements are not included. The dashed line represents a one-to-one correspondence between cometary and ISM abundances and is not a fit to the data.

Figures 3.20 and 3.21 compare the cometary abundances from Bockelée-Morvan et al. (2000, 2004) to the abundances from our model at the end of the collapse phase. The horizontal error bars show again the spread in abundances between individual comets. In Fig. 3.20, the vertical error bars show the spread across our entire disk; in Fig. 3.21, they show the spread in the 5–30 AU region at the midplane. For all species, the gas and ice abundances from the model are summed and displayed as one.

The disk-wide abundances tend to cluster around the theoretical one-to-one relationship indicated by the dotted line. Two notable exceptions are CH_3OH and $HCOOCH_3$. Both of them are known to require grain-surface chemistry to get the correct abundance, and this is not included in our model. The spread in model abundances is at least six orders of magnitude, but given the wide range of physical conditions that are sampled, such a large spread is to be expected. The 5–30 AU abundances from Fig. 3.21 show less variation – between one and four orders of magnitude – but still take on a wider range of values than do the cometary abundances. More importantly, the 5–30 AU data show no

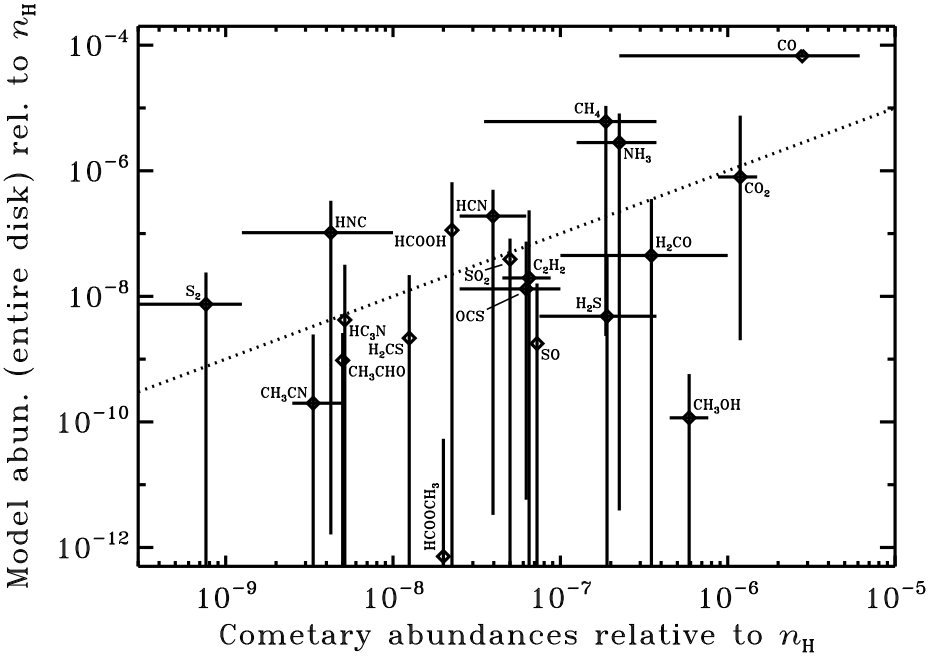

Figure 3.20 – As Fig. 3.19, but comparing the cometary abundances to those in our model at $t = t_{acc}$. The vertical black lines indicate the spread across the entire disk. For all species, the gas and ice abundances from the model are summed and displayed as one.

correlation with the comet data. There is no indication from Sect. 3.6 that post-collapse processing brings the abundances back to near-ISM values. Hence, the midplane material between 5 and 30 AU in our model does not appear to be analogous to the material from which the solar-system comets originated.

How plausible is the large degree of chemical processing for material that ends up in the comet-forming zone? The amount of processing is a direct result of the range of physical conditions encountered along a given infall trajectory, which in turn depends mostly on how close to the protostar the trajectory gets. We intentionally keep the physics in our model as simple as possible, so a trajectory like the one drawn in Fig. 3.5 may not be fully realistic. On the other hand, the back-and-forth motion results from the well-known concept of conservation of angular momentum. As the inner parts of the disk accrete onto the star, the outer parts must move out to maintain the overall angular momentum. They may be pushed inwards again at a later time if a sufficient amount of mass is accreted from the envelope at larger radii. This happens in our simple model, but also in the hydrodynamical simulations of Brinch et al. (2008a,b).

If we accept the possibility of back-and-forth motion, the question remains as to how close to the star the material gets before moving out to colder parts of the disk. Our

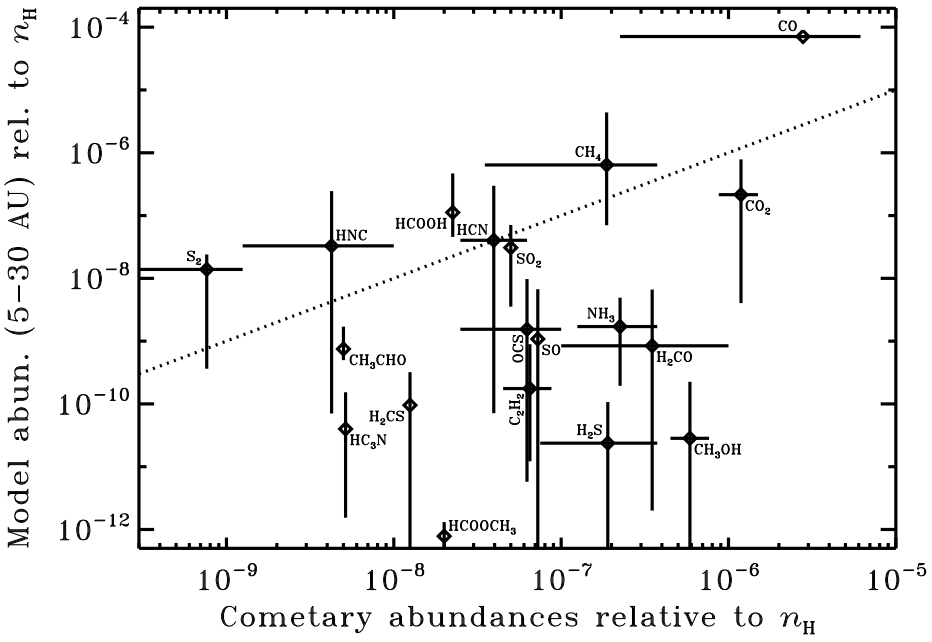

Figure 3.21 – As Fig. 3.19, but comparing the cometary abundances to those in our model at $t = t_{\rm acc}$. The vertical black lines indicate the spread in the comet-forming region: at the midplane, between 5 and 30 AU from the star.

new solution to the problem of sub-Keplerian accretion (see Chapter 4) results in radial velocity profiles that are different from the ones in Chapter 2. With the old profiles, all material that accretes inside of the snow line always remains inside of the snow line. We therefore did not get any material in the comet-forming zone in which H_2O had evaporated and readsorbed onto the grains. As shown in Fig. 3.5, we do get this with our current model. However, it is not a universal outcome for all initial physical conditions. If we run the new model on the parameter grid from Chapter 2, there are three cases (out of eight) where material accretes inside of the snow line and then moves out beyond it. The dividing factor appears to be a ratio of 0.2 between the disk mass at $t = t_{\rm acc}$ and the core mass at $t = 0$. For larger ratios, material that accretes inside of the snow line always remains there.

The presence of crystalline silicate dust in disks provides a strong argument in favour of trajectories like the one from Fig. 3.5. Observations show crystalline fractions at $R \approx 10$ AU that are significantly larger than what is found in the ISM (Bouwman et al. 2001, 2008, van Boekel et al. 2005). Amorphous silicates can be crystallised by thermal annealing if they get close enough to the star to be heated to at least 800 K. The disk is less than 100 K at 10 AU, so the crystalline dust is formed at smaller radii than where it is ob-

served. We argue in Chapter 4 that the need to conserve angular momentum results in the outward transport of enough material to explain the observed crystalline fractions at 10 AU. Moreover, crystalline dust has been detected in several comets, including 1P/Halley, C/1995 01 (Hale-Bopp) and 81P/Wild 2, providing direct evidence that part of their constituent material has been heated to temperatures well above the evaporation temperature of H_2O (Bregman et al. 1987, Campins & Ryan 1989, Wooden et al. 1999, Keller et al. 2006).

If Halley, Hale-Bopp, Wild 2 and other comets contain crystalline silicates, they must also contain ices that underwent a large degree of chemical processing. Likewise, the presence of amorphous silicates in comets is indicative of chemically unprocessed ices. Hence, we conclude that the material from which comets are formed must be of mixed origins: some of it accreted close to the star and was heated to high temperatures, while another part accreted at larger radii and remained cold. Within the context of our model, this requires that material from beyond $R = 30$ AU is radially mixed into the comet-forming zone between 5 and 30 AU. Alternatively, vertical mixing may bring relatively pristine material from higher altitudes down into the comet-forming zone at the mid-plane. As for the chemical variations between individual comets, our model shows many examples of abundances changing with position or with time. The variations can thus be explained by having the comets form at different positions in the circumsolar disk, or at different times during the disk's lifetime.

3.7.3 Collapse models: 1D versus 2D

The model presented here and in Chapter 2 is the first one to follow the entire core collapse and disk formation process in two spatial dimensions. Some of our conclusions were previously drawn in other studies on the basis of 1D models. For example, it was already known that the collapse-phase chemistry is dominated by a few key chemical processes and that the collapsing core never attains chemical equilibrium (e.g., Doty et al. 2002, 2004, Rodgers & Charnley 2003, Lee et al. 2004, Aikawa et al. 2008). The 1D models cannot follow the infalling material all the way into the disk, so the zones with different chemical histories from Sect. 3.6 appear for the first time in our 2D model. Another new feature is the back-and-forth motion inside the disk, allowing material to accrete inside of the snow line and then move out to colder regions. This offers new insights into the chemical origin of cometary nuclei.

3.8 Conclusions

This chapter describes the two-dimensional chemical evolution during the collapse of a molecular cloud core to form a low-mass star and a circumstellar disk. The model is the same as used in Chapter 2, except for the improvements described in Chapter 4. The density and velocity profiles throughout the core and the disk are computed semi-analytically. We use a full radiative transfer method for the dust temperature and the radiation field. The chemistry is computed with a full gas-phase network, including adsorption and des-

orption from dust grains, as well as basic hydrogenation reactions on the grain surfaces. Starting from realistic initial conditions, we evolve the chemistry in parcels of material terminating at a range of positions in the disk. Special attention is paid to parcels ending up in the comet-forming zone. The conclusions from this chapter are as follows:

- The chemistry during the collapse phase is controlled by a small number of key chemical processes, each of which is activated by changes in the physical conditions. The evaporation of CO, CH_4 and H_2O at approximately 18, 22 and 100 K is one set of such key processes. Another set is the photodissociation of CH_4 and H_2O (Sect. 3.5.1).
- At the end of the collapse phase, the disk can be divided into several zones with different chemical histories. The different histories are related to the presence or absence of the aforementioned key processes along various infall trajectories. Spectroscopic observations at high spatial resolution are required to determine whether this zonal division really exists, or if it is smoothed out by mixing (Sect. 3.5.2).
- Part of the material that accretes onto the disk at early times is transported outwards to conserve angular momentum, and may remain in the disk for the rest of the collapse phase. It is heated to well above 100 K as it accretes close to the star, so H_2O and all other non-refractory species evaporate from the grains. They freeze out again when the material cools down during the subsequent outward transport (Sect. 3.5.2).
- When the chemistry is evolved for an additional 1 Myr at fixed physical conditions after the end of the collapse phase, the abundances of most species change throughout the disk. Hence, the disk is not in chemical equilibrium at the end of the collapse. Instead, its chemical composition is mainly a result of the physical conditions during the collapse phase. A robust feature of the post-collapse processing is the partial conversion of gaseous CH_4 into larger species like HCOOH or C_3H_4, which subsequently freeze out because of their higher binding energy (Sect. 3.6).
- Material that ends up in the comet-forming zone undergoes a large degree of chemical processing, including the evaporation and readsorption of H_2O and species trapped in the H_2O ice. This is consistent with the presence of crystalline silicates in comets. However, it is inconsistent with the chemical similarities observed between comets and ISM sources, which are indicative of little processing. Hence, it appears that the cometary material is of mixed origins: part of it was strongly processed, and part of it was not. The chemical variations observed between individual comets suggest they were formed at different positions or times in the solar nebula. Fully pristine ices only appear in the upper and outer parts of this particular disk model (Sect. 3.7.2).